International Journal of Mechanical Sciences 287 (2025) 109955

Contents lists available at ScienceDirect

International Journal of Mechanical Sciences

journal homepage: www.elsevier.com/locate/ijmecsci

Fatigue-creep design of transpiration cooled nickel gas turbine blades via low order aerothermal-stress and crystal plasticity finite element modelling

Christos Skamniotis [a,*], Michael van de Noort [b], Alan C.F. Cocks [b], Peter Ireland [b]

[a] Department of Engineering, King's College London, WC2R 2LS, UK
[b] Department of Engineering Science, University of Oxford, Oxford OX1 3PJ, UK

ARTICLE INFO

Keywords:
Transpiration cooling
Nickel-based gas turbine blades
Fatigue-creep
Crystal plasticity finite element modelling
Thermomechanical stresses

ABSTRACT

Transpiration Cooling (TC) systems can substantially improve the fuel efficiency of jet engines by allowing them to run much hotter than current designs allow. However, TC systems require radically new designs where large cyclic thermomechanical stresses and creep-plastic deformation can limit the life of core components. This can only be mitigated through integrated design approaches which simultaneously consider the aerothermal and mechanical performance. We develop here a low order aerothermal-stress model (LOM) which combines first order coolant flow and fluid-solid convective-conductive heat transfer calculations with stress calculations in the solid. The LOM provides rapid answers to crucial design questions: how much cooling air and how many cooling holes are required in gas turbine blades for them to operate safely at a given turbine inlet (hot gas) temperature? The LOM also narrows the range of conditions under which Crystal Plasticity Finite Element (CPFE) simulations may be required for fatigue-creep life assessment at final design stages. Our answer to previous pessimistic views on the practical use of TC is that TC systems can actually work thanks to the threefold benefit of cooling holes in reducing metal temperatures, temperature gradients and effective thermal stresses. CPFE simulations confirm this new conclusion, encouraging the wider use of our hybrid design strategy in turbomachines, hypersonic technologies and fusion reactors as well as the take-up of TC systems to deliver durable hydrogen-fuelled turbines for Net Zero.

1. Introduction

The need to increase the operating temperature of aero-engines and land-based turbines to boost their fuel efficiency is ongoing [1–3]. The further development of advanced Nickel superalloys and thermal barrier coatings offers limited scope for increasing turbine inlet temperatures from current levels [1,2]. A more promising approach is through the invention of clever cooling systems [4,5]. Innovative ways of manipulating hot and cold air flows need to be found in order to cool critical components that are surrounded by gas temperatures well beyond their melting point [6]. The transpiration cooling (TC) system in Fig. 1a, 1b1-b2 is one such innovation where arrays of film holes are used to blow coolant air externally to repel the hot gas flow away from the metal surface, while the two walls allow as much heat as possible to be transferred to the coolant before it escapes [7].

Recent theoretical developments and experimental studies [8–15] indicate that TC systems can deliver significant enhancements in convective efficiency and cooling effectiveness, but these benefits come with a number of challenges. TC systems must utilise a minimum coolant volume to maximise the amount of air that is available for combustion and they must also be competitive with other systems in terms of mechanical performance and manufacturability [16]. So far, cooling and structural mechanics have worked together synergistically, since the former serves to maintain low component temperatures and temperature gradients which both limit thermal stresses to improve mechanical performance [3].

However, in order to combat extreme gas temperatures, TC systems provide enhanced cooling which demands unusual geometric features, including multi-walls and inclined holes which behave like elliptical cracks [9,17]. The interaction between thermally mismatching walls induces high bulk thermal stresses [18], which are enhanced by the increase of thermal expansion coefficient of Nickel superalloys with temperature (see Fig. 2a) [19] and further intensify to critical levels locally at stress raising features, i.e., cooling holes [20]. These severe stress magnitudes generated locally cannot be accommodated by the material but rather must be contained within the material specific yield limit. Nickel superalloys, for instance, exhibit a decreasing yield stress at high temperatures beyond 800 °C (see Fig. 2b), and as a result, the

---

* Corresponding author.

https://doi.org/10.1016/j.ijmecsci.2025.109955
Received 8 May 2024; Received in revised form 6 January 2025; Accepted 7 January 2025

material at the vicinity of cooling holes can locally experience excessive plastic deformation during engine startup (heat-up), accompanied by the slower creep deformation and strain softening effects during steady state high temperature operation (see Fig. 2c). Both plasticity and creep result in severe local residual stresses which, in turn, can drive yield and low temperature plastic deformation in the reverse direction during engine shutdown (cooldown) [21,22]. These deformation reversals, typically underpinned by creep at high temperature operation and plasticity at low temperature shutdown, cause damage and can lead to crack development within a very low number of service cycles, widely known as low cycle fatigue failure [21,22].

The above conflict between cooling and mechanical design currently presents the biggest obstacle to the adoption of TC systems [22], along with the concerns around sensitivity to manufacturing variations [23], excessive coolant demand and hot gas ingestion [24]. These aspects have not received the attention they deserve. Most studies have focused on the fluid science of TC systems to understand coolant flow and predict metal temperatures [7,8,25–32] through modelling and experiments. Considerable attention has also been given to thermomechanical stresses and the severity of fatigue-creep failure in Nickel superalloys, investigated by destructive experiments and Crystal Plasticity Finite Element (CPFE) simulations using simple thermomechanical loading histories, geometries and material models [33–41]. Recently, the authors addressed these shortcomings via a series of investigations [9,17–22,42–44] (summarised in Fig. 1), all underpinned by one central approach: the steady state temperature field is determined via coolant flow CFD simulations (Fig. 1b1) and subsequent FE heat conduction analyses (Fig. 1b2) [9,17]; this is then used as input in theoretical-FE thermoelastic stress analysis (Fig. 1c1-c3) and subsequent cyclic inelastic CPFE analysis (Fig. 1d1-d3) using the key elastic-plastic-creep properties of Nickel superalloys shown in Fig. 2a–c. Elastic stress analysis helps understand the nature of thermal-centrifugal stresses and associated kinematic constraints via full component FE models (Fig. 1c1) [17] and 2D-3D theoretical-FE unit cell models (Fig. 1c2-c3) [18,43], as well as determine how these stresses intensify at cooling features (Fig. 1c2) [19,20]. Inelastic analysis determines the thermal-centrifugal load regimes where fatigue, creep and ratchetting failure modes dominate (Fig. 1d1) [42,44], and predicts local creep-plastic deformation and fatigue at stress concentrating feature via CPFE simulations (Fig. 1d2-d3) [22] or pseudo-analytical Neuber-type

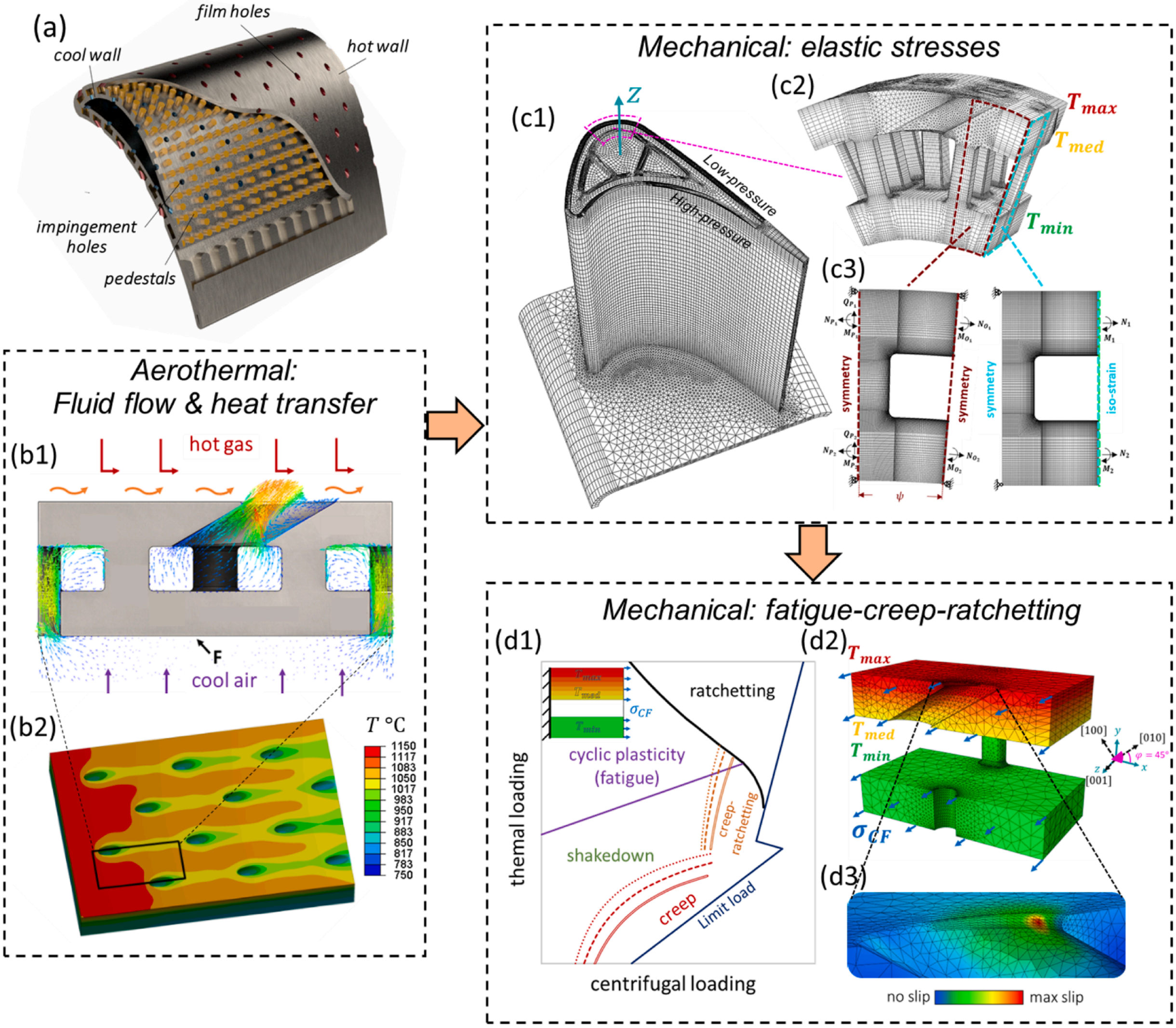

Fig. 1. Summary of computational studies on twin wall transpiration cooled (TC) turbine blades. **a** example of a TC blade [45]. **b1** unit cell of a TC turbine blade showing coolant velocity-temperature CFD patterns [22]. **b2** temperature field from heat transfer analysis [17]. **c1** turbine blade FE model for determining elastic bulk wall stresses [17]. **c2** unit cell FE model of blade suction region for determining elastic stresses at holes and pedestals. **c3** Analytical-FE 2D models for studying the effect of kinematic constraints on thermal stresses [43]. **d1** interaction diagram (Bree type) showing dominant cyclic failure mechanisms for varying thermal-centrifugal load amplitudes (2D shakedown analysis) [42,44]. **d2** CPFE model for predicting inelastic deformation and fatigue-creep life at holes under cyclic loading [22]. **d3** qualitative slip localisation contours at film hole.

schemes [21].

The consensus is that the combination of high temperature and stress at cooling holes results in fatigue failure after only a small number of service cycles, suggesting unacceptably short life expectancy for TC systems. Here we will demonstrate that such a conclusion can be overly pessimistic. The crucial factor that changes our opinion is the density of film cooling holes, a factor which has not been explored on a firm quantitative basis in the open literature. We will show that wall porosity induces synergy between cooling and mechanical response, since it not only reduces the temperature magnitudes and their gradients, but also the effective turbine blade wall stiffness, and since thermally generated stresses are displacement controlled, this leads to lower hole stresses. A natural question that immediately follows is: “how much porosity and coolant flow are required for these stresses to become low enough such that fatigue is not an issue?” If we think conservatively, we postulate that fatigue is completely avoided. If we think less conservatively, we demand that fatigue crack initiation occurs after a sufficiently large number of cycles. If we think non-conservatively, we require that cracks propagate slowly or arrest such that crack initiation does not mean early catastrophic failure. We will show here that in contrast to the last two incremental approaches which require a completely new boundary value problem to be solved for each combination of conditions, e.g., a full cyclic CPFE simulation for each case, the first approach is far more suited to answer the above question because it can be implemented iteratively via simplified and fast calculations of coolant mass flow, heat transfer and stress.

These calculations will lead to a new framework which we refer to as a ‘low order aerothermal-stress model’ or equivalently ‘low order mass-heat transfer-stress model’ (LOM), which facilitates rapid communication between the cooling and the mechanical perspectives such that a balance between the two can be readily achieved in design. Evidence will be presented to demonstrate that if this balance is achieved, TC systems can allow turbine blades to withstand extreme hot gas flow temperatures without jeopardising the engine integrity. The latter is validated by detailed CPFE simulations and fatigue-creep life assessment under a particular set of conditions chosen based on the LOM results, which will simultaneously showcase the unprecedented capability of the LOM to effectively guide elaborate numerical/computational analyses and life prediction schemes. This study supports the internationally growing research activity on TC systems, the need for cost-effective design guide tools and the strong industrial drive for TC systems to be employed in future engines and hypersonic technologies.

Section 2 describes the aerothermal-stress calculations underpinning the LOM framework and presents the quantitative interplay between cooling conditions, component geometry and stress. Section 3 describes the key features of the damaging behaviour at the cooling holes of a TC system predicted via CPFE and shows how the severity of fatigue-creep damage can be predicted through the LOM – this leads to the novel design diagrams in Fig. 8 as the major output of this paper. Section 4 then discusses our results and methods and identifies future research directions, followed by our major conclusions in Section 5.

2. Low order aerothermal-stress model (LOM)

Fig. 3 summarises the workflow of the newly developed aerothermal-stress model (LOM), which builds on our previous fluid flow, heat transfer, thermomechanical stress and fatigue-creep-ratchetting failure studies described in the Introduction and illustrated in Fig. 1. In this paper we will utilise the LOM for the case of a planar unit of a TC system, which is representative of the low-pressure side of gas turbine blades. The following sub-sections describe the sequence of mass flow, heat transfer and stress calculations underpinning this problem, by focusing on the physical essence of the results and their practical implications for design. The details of calculations are described in the Appendix.

2.1. Aerothermal calculation

The aerothermal code of the LOM is illustrated in Fig. 4a and b. The code was originally developed and validated by the authors recently in [24,50] and its calculation details are given here in Appendix A. In brief, these calculations concern the: a) mass flow and static pressure fields throughout the fluid domain, and b) energy flow and steady state temperature fields throughout the solid and fluid domains. The efficiency-speed of these calculations lies in the discretisation of TC systems into one-dimensional (1D) mass-heat flow elements. Of course, this discretisation does limit the accuracy of the model in comparison to higher-fidelity CFD simulations, particularly in complex flow-fields. The advantage of the LOM here is that the form of the flow-field in a flat TC system is relatively simple and consistent with the flow network formation. This remains the case across the entire range of porosities investigated here, i.e. up to 20% outer wall porosity. Future work will explore the trade-off between computational accuracy and efficiency for cases of more complex flow-fields through comparing results between LOM and full CFD simulations.

The full aerothermal fields are produced and solved for the entire TC system shown in Fig. 4b by repeating and mirroring accordingly the calculations performed within the unit cell of Fig. 4a. As indicated in Fig. 3a, the code uses the input parameters listed in Table 1, describing the gas turbine (mainstream) hot gas flow $\mathscr{T}$={external heat transfer coefficient h_∞, temperature T_∞, pressure p_∞, velocity v_∞}, the coolant

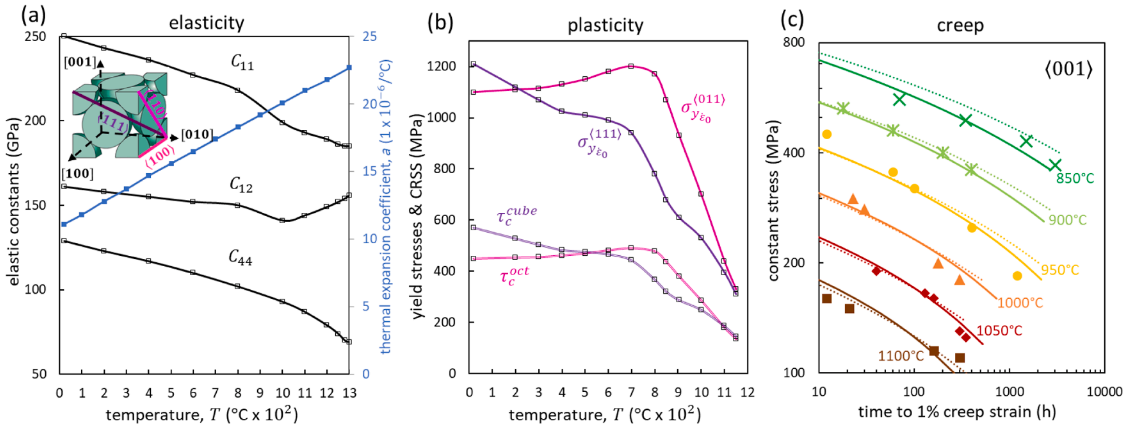

Fig. 2. Summary of temperature dependent properties of the CMSX-4 Nickel superalloy. **a** variation of elastic constants [46] and thermal expansion coefficient [47] with temperature. **b** variation of macroscopic yield strength along ⟨001⟩ and ⟨111⟩ crystallographic directions and the related critical resolved shear stresses (CRSS) for octahedral and cubic slip with temperature [48]. **c** time to 1 % creep strain for various constant stresses and temperatures for loading along the ⟨001⟩ crystallographic direction [49].

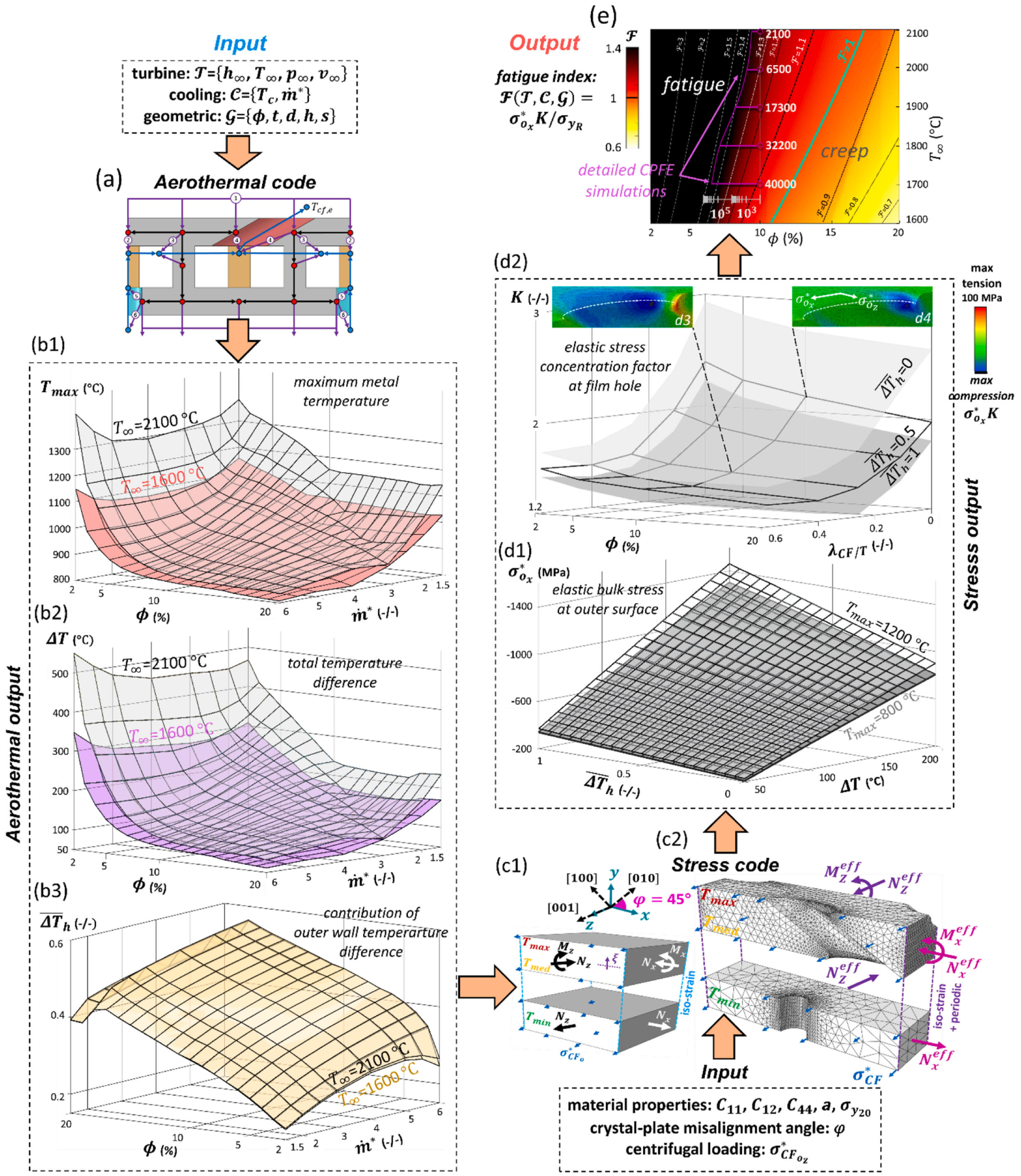

Fig. 3. Illustration of low order aerothermal-stress model (LOM). **a** aerothermal code of the LOM, using input parameters to output temperature field via pseudo-analytical analysis of coolant mass flow and heat transfer. **b1-b3** variation of temperature field parameters (max temperature T_{max}, total temperature difference ΔT, outer wall temperature difference contribution $\overline{\Delta T}_h$) with respect to outer wall porosity Φ, coolant mass flow rate m^*, hot gas temperature T_∞. **c1-c2** stress code of the LOM, using T_{max},ΔT, $\overline{\Delta T}_h$ as input to output elastic bulk stress at outer metal surface $\sigma^*_{o_x}$ via analytical coupled elastic plate analysis (c) and elastic stress concentration factor K at film hole via one-off FE analysis (c2). **d1** variation of $\sigma^*_{o_x}$ with $\overline{\Delta T}_h$, ΔT, T_{max}. **d2** variation of K with Φ, $\overline{\Delta T}_h$ and the centrifugal to thermal stress ratio $\lambda_{CF/T} = \sigma^*_{CF_{o_z}} / \left|\sigma^*_{T_{o_x}}\right|$. **d3-d4** comparison of elastic FE stress concentrations at film holes for two $\lambda_{CF/T}$ ratio. **e** output of LOM in terms of a design diagram showing the variation of fatigue index $\mathscr{F}$ with respect to T_∞ and Φ, which indicates the regimes where fatigue (low cycle fatigue) and pure creep behaviour prevail at the hot spot location of the cooling hole.

flow $\mathscr{C}$= {coolant temperature T_c, dimensionless flow rate $\dot m^*$}, and the TC geometry $\mathscr{G}$= {outer wall porosity ϕ, wall thicknesses t, hole diameters d, pedestal size parameters h={H, l, w}, hole spacing ratio s}. Here we define $\dot m^* = (\dot m_{cf} c_p)/(h_\infty A)$, where A is the total area of the external/hot surface of the TC system in Fig. 4b, $\dot m_{cf}$ is the total coolant mass flow and c_p=1006 J/kg K is the air specific heat capacity. The above definition of m* includes h_∞ as a way of making it non-dimensional. In our parametric studies here when we modify the outer wall porosity of the TC system (by reducing the spacing between film holes) we also modify the external surface area A accordingly such that

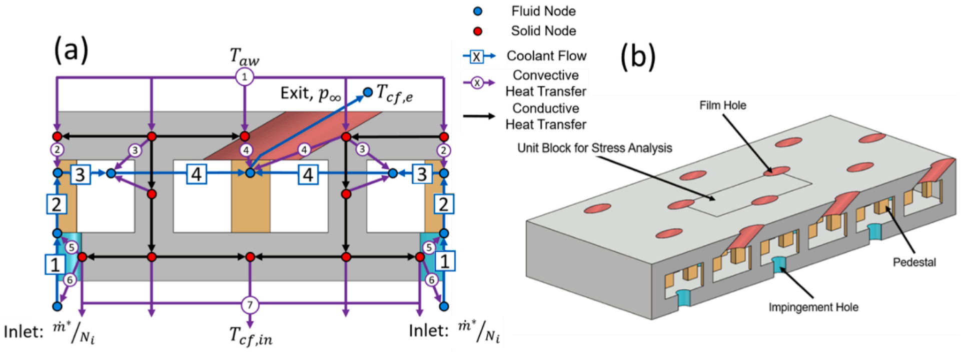

Fig. 4. Illustration of the aerothermal code of the LOM. **a** mass flow and heat flow networks for a repeating unit cell of a planar transpiration cooling system (TC). The networks discretise coolant flow and heat flow by identifying fluid node locations, flow link compliances as well as convective and conductive heat transfer links. Boundary conditions are shown at the coolant inlet with non-dimensional mass flow $\dot{m}^*/N_i$ and temperature $T_{cf,in}$ as well as the coolant exit with pressure p_∞ and temperature $T_{cf,e}$; the latter is a free variable (non-prescribed). **b** TC system used for the full aerothermal calculation, from which the repeating unit cell referenced as 'unit block for stress analysis' is finally used in Fig. 4a and in the stress code in Fig. 3c2.

Table 1
Summary of input parameters used in the low order aerothermal-stress model (LOM).

Turbine parameters	Notation	Value
external heat transfer coefficient	h_∞	7.5 kW/m^2 K
hot gas (mainstream) temperature	T_∞	varies between 1600 and 2100 °C
hot gas pressure	p_∞	3.4 MPa
hot gas velocity	v_∞	500 m/s
cooling parameters		
coolant temperature	T_c	1000 K
dimensionless coolant flow rate	m^*	varies between 3 and 6
transpiration cooling geometry parameters		
outer wall porosity	ϕ	varies between 2 and 20 %
hot (outer) wall thickness	t_h	1 mm
cool (inner) wall thickness	t_c	0.8 mm (0.4 mm used in Fig. 7d)
film/impingement hole diameter	d	0.6 mm
pedestal height	H	1 mm
pedestal length	l	0.48 mm
pedestal width	w	0.24 mm
ratio of streamwise to spanwise hole spacing	s	2
film hole fillet radius	ρ	0.05 mm

different porosities can be compared for the same m* to ensure a consistent coolant mass flow to external surface area ratio (c_p and h_∞ are constant throughout). The reason why h_∞ is kept constant throughout our parametric studies is because we want to isolate the effect of an intensifying thermal load without introducing too many variables; for the same reason, the mainstream pressure p_∞ and velocity v_∞ are also kept constant. In practise, when the hot mainstream temperature changes T_∞ then also h_∞, p_∞ and v_∞ change. In reality, variation of T_∞ will change the hot gas density ρ_∞, which influences the blowing ratio and therefore the external cooling performance as demonstrated in Appendix A.

The key output of the aerothermal code is the steady state temperature field throughout the solid volume of the TC system, which is fully represented here by Figs. 3b1-b3; while the TC system consists of several repeating unit cells, here we focus on the temperature field within the single representative unit cell denoted in Fig. 4a. We have ensured that this simplified code produces temperature fields consistent with the ones shown in Fig. 1b1-b2 determined from elaborate CFD-heat transfer analysis [17]. The main feature of these fields is that temperatures vary in an approximately linear manner through the outer wall thickness and pedestal height and the inner wall experiences a uniform temperature T_{min}. Hence, with negligible loss of accuracy, temperature fields are described by only three quantities: T_{max} (maximum metal temperature at the outer surface), $\Delta T = T_{max} - T_{min}$ (total temperature difference in the TC system) and $\overline{\Delta T}_h = (T_{max} - T_{med})/\Delta T$ (contribution of outer wall temperature difference to total difference). As Fig. 3b1-b3 indicate, these fields are greatly influenced by the hot gas temperature T_∞, outer wall porosity Φ and dimensionless coolant mass flow rate $\dot{m}^*$. T_{max} and ΔT are found to reduce exponentially with ϕ (Fig. 3b1-b2), whereas the opposite occurs for $\overline{\Delta T}_h$ (Fig. 3b3).

As porosity increases, the contribution of each internal cooling mechanism to the overall cooling is modified. At low porosities, the impingement cooling throughout the internal surface of the hot wall dominates. However, as porosity increases the spacing between cooling features reduces, which in turn reduces the area available for impingement cooling. At high porosities, the dominant contributions to internal cooling are coming from the in-hole film cooling in the outer hot wall and pedestal cooling, as the area available for both does not change with porosity here. Similar trends were observed in [51]. The higher density of features at high porosities is also found here to improve the t cooling performance, evidenced by the lower values of $T_{max}$and ΔT in Fig. 3b1 and Fig. 3b2 respectively and higher values of $\overline{\Delta T}_h$ in Fig. 3b3 than those at lower porosities. $\dot{m}^*$ only has a significant influence on T_{max} (Fig. 3b1), and as expected, $\overline{\Delta T}_h$ is insensitive to T_∞ (results for different T_∞ collapse onto the surface shown in Fig. 3b3) since the form of the temperature field is independent of the temperature magnitudes involved. In contrast to $\overline{\Delta T}_h$, both T_{max} and ΔT are absolute quantities and therefore are heavily dependent on T_∞, as shown by the two surfaces for the extremes of temperature T_∞=1600 °C and T_∞=2100 °C considered in Fig. 3b1-b2; the dependence has been observed to be linear, i.e. T_{max} and ΔT surfaces for intermediate T_∞ values can be accurately determined by linear interpolation.

2.2. Stress calculation

2.2.1. Bulk elastic stresses

The aerothermal output of the LOM, i.e., the temperature field parameters T_{max},ΔT, $\overline{\Delta T}_h$, are inputted into the stress code of the LOM illustrated in Fig. 3c1-c2. The efficiency-speed of the underlying stress calculations lies in the consideration of a purely elastic material response, i.e., the ignorance of local non-linearities in the structure posed by plastic and creep deformation. The first step of the stress code is to compute rapidly the bulk thermal stresses $\sigma^*_{T_o}$ in the two walls of the TC array by utilising the analytical elastic stress solution/model for thermally mismatching walls illustrated in Fig. 3c1, as a function of the full temperature dependent elastic-thermal properties of Nickel superalloys shown in Fig. 2a. Wall connecting pedestals are not explicitly included in the code as they exhibit stresses of secondary importance

[22]. However, their kinematic coupling effect on the walls is captured via the isostrain condition which is responsible for the generation of severe compressive thermal stresses in the outer wall, balanced by tensile thermal stresses in the inner wall. The outer wall sees additional bending stresses that scale with the temperature difference T_{max}-T_{med} and hence the $\overline{\Delta T}_h$ ratio, which means that the outer surface (where T_{max} applies) experiences the maximum thermal stress magnitudes in the system. We will focus on this location and examine the critical case when the x-stress component $\sigma^*_{o_x}$ is much more severe than the z-component $\sigma^*_{o_z}$ because the x axis aligns with the stiff crystallographic orientation ⟨011⟩ (see rotated crystal system with respect to global plate *xyz* system in Fig. 3c1) [9]. Fig. 3d1 shows the variation of $\sigma^*_{o_x}$ with T_{max}, ΔT, $\overline{\Delta T}_h$. The stress $\sigma^*_{o_x}$ increases in a linear manner with both ΔT and $\overline{\Delta T}_h$, with $\overline{\Delta T}_h$ having a smaller influence as it only changes the contribution of bending to the stress distribution in the outer wall, as opposed to ΔT which scales the entire stress field. $\sigma^*_{o_x}$ also increases as the magnitudes of the temperatures, represented by T_{max}, increase because the elevation of thermal expansion coefficient a with increasing temperature in Nickel dominates over the reduction in material stiffness [9]; however, the change of these properties in the range of interest 800 °C<T_{max}<1200 °C is small, explaining the weak dependence of $\sigma^*_{o_x}$ on T_{max}.

2.2.2. Local elastic stresses

The second step of the stress code is to multiply the bulk stress at the outer surface determined by the model in Fig. 3c1 by an elastic stress concentration factor K to predict the intensified (peak) elastic stress in the vicinity of the film hole ($\sigma^*=\sigma^*_{o_x}K$); this is possible by utilising the elastic FE model in Fig. 3c2. K is independent of T_{max} and ΔT but depends heavily on three parameters: film hole density (represented here by ϕ), contribution of bending to the outer wall stress distribution (represented here by $\overline{\Delta T}_h$) and biaxial stress ratio at the outer surface $\sigma^*_{o_z}/\sigma^*_{o_x}$ (represented here by the ratio of centrifugal stress applied to the net wall section to the bulk thermal x-stress magnitude $\lambda_{CF/T} = \sigma^*_{CF_z} / \left|\sigma^*_{T_{o_x}}\right|$). An analytical calculation of K is not possible, but the elastic FE analysis in Fig. 3c2 can straightforwardly provide the unknown peak stress σ*, which together with the theoretical bulk stress $\sigma^*_{o_x}$ can be used to determine K. Performing a one-off set of 60 FE simulations (5 $\lambda_{CF/T}$ values x 4 Φ x 3 $\overline{\Delta T}_h$) using the model in Fig. 3c2 leads to the three surfaces describing the K factor that are plotted in Fig. 3d2. It can be seen that K minimises as $\overline{\Delta T}_h$ decreases to 1 because enhanced bulk stress gradients through the outer wall thickness obstruct the development of additional stress gradients near surface cavities; this phenomenon has been demonstrated recently by the authors [20] by indicating that the stress concentration factor at the rim of a hole in a hole-plate structure is lower when the bulk stress distribution is uniformly tensile/compressive through the plate thickness than when the bulk stress distribution is non-uniform and varies linearly through the plate thickness, i.e. bending stress distribution.

Fig. 3d2 also shows that K reduces with increasing $\lambda_{CF/T}$ ratio because the tensile centrifugal stress $\sigma^*_{CF_z}$ reduces the magnitude of the total compressive bulk stress $\sigma^*_{o_z}$, such that the very high bulk compressive stress $\sigma^*_{o_x}$ dictates the stress concentration around the hole [22]; $\sigma^*_{o_x}$ drives the local stresses to concentrate near the low curvature (co-vertex) region of the elliptical cavity formed in the plane of the wall by the inclined cooling hole (Fig. 2d3) and hence to distribute over a larger volume compared to the case $\lambda_{CF/T}$=0 when concentration occurs near the elliptical vertex (Fig. 2d4). We note that the $\sigma^*_{CF_z}$ value in the calculation of $\lambda_{CF/T}$ concerns the net wall section, such that high porosity ϕ for fixed $\sigma^*_{CF_z}$ corresponds to high bulk/gross centrifugal stress $\sigma^*_{CF_{o_z}}$; this suggests that all the above effects are generally enhanced in porous turbine blades.

2.2.3. Effect of porosity on stresses

The third and most interesting effect is the reduction of stress concentration factor K with hot wall porosity ϕ (see Fig. 3d2). An increasing ϕ implicitly reduces the proximity between adjacent holes, which in turn has been suggested to attenuate the stress gradients and thus peak stresses at the vicinity of holes, known as 'hole-hole interaction' effect [20]. However, this effect has not been rigorously quantified until now, and its significance remains unknown for compound holes under the different stress gradients involved in thermal loading and mechanical loading. In this study, we provide evidence that the dominant mechanism by which ϕ influences K, is the reduction of the 'effective' plate stiffness due to the material removed by the holes rather than the hole–hole interaction effect. Considering pure thermal loading (displacement controlled), the reduction of effective plate stiffness in principle implies a proportional reduction in the volume averaged (effective) thermal stress $\sigma^{*eff}_{o_x}$ which is suggested here to drive the reduction of K with increasing ϕ.

It is instructive now to consider that K in Fig. 3d2 is defined based on the bulk stress ($\sigma^*=\sigma^*_{o_x}K$), which does not immediately indicate the contribution of effective thermal stress reduction to the reduction of K with increasing ϕ. To indicate this role, we must utilise a different definition for the stress concentration factor based on effective stress, i.e. $\sigma^*=\sigma^{*eff}_{o_x}K^{eff}$, in which case K^{eff} is only influenced by stress gradient effects. Comparison of the two definitions (K and K^{eff}) in Fig. 5a reveals that while K decays with porosity ϕ, K^{eff} actually increases, indicating that stress gradients in the vicinity of holes intensify as adjacent holes come into closer proximity (increasing ϕ inherently reduces hole-hole proximity); data presented here concerns the film hole of the FE model in the inset Fig. 5c' (equivalent to Fig. 3c2), as well as the circular holes of the constrained 2D isotropic porous plate model in Fig. 5b under uniform temperature loading. It is revealed that in thermal loading problems, the porosity ϕ imposes a competition between stress gradient elevation and effective stress reduction, with the latter dominating. This analysis would not have been possible without the calculation of $\sigma^{*eff}_{o_x}$ for each ϕ value. The volume averaged forces and moments used to deduce $\sigma^{*eff}_{o_x}$ for the problem of Fig. 5c' (or equivalently Fig. 3c2) are plotted in Fig. 5c and are normalised by the respective bulk values determined from Fig. 3c1. FE results agree with the analytical Tsukrov–Kashanov model for 2D orthotropic porous plates [52,53], both highlighting the dominant, beneficial effect of porosity, along with its anisotropic nature, i.e. z components reduce more than x components due to the in-plane ellipticity induced by the film holes. The reduction of moments scales only with the outer wall porosity Φ, whereas the reduction of forces scales with the average porosity of the two walls; the porosity range 2–30 % in the outer wall of Fig. 5c and d here compares to a smaller 2–7 % range in the inner wall, which explains why forces reduce less than moments. Finally, it should be noted here that all the above results surrounding the reduction of effective plate stiffness with increasing porosity concern the purely elastic regime and thermal loading (displacement controlled) but not mechanical loading (force controlled); as shown in [54] the internal strain gradients (and thus also stress gradients) experienced in porous structures differ significantly between thermal loading and mechanical loading. With finally emphasise that all the above results correspond to the purely elastic regime.

3. Design diagram and life assessment

Once we have captured all possible variations of the elastic stress concentration factor K, the LOM can now rapidly calculate the peak elastic stress $\sigma^*=\sigma^*_{o_x}K$ for any given set of turbine, cooling and geometric parameters. We will show here that although the quantity σ* completely ignores the local material plastic-creep deformation encountered in practise, it can be readily used to indicate whether low cycle fatigue failure can occur and provide the relevant design diagram in Fig. 3e, as

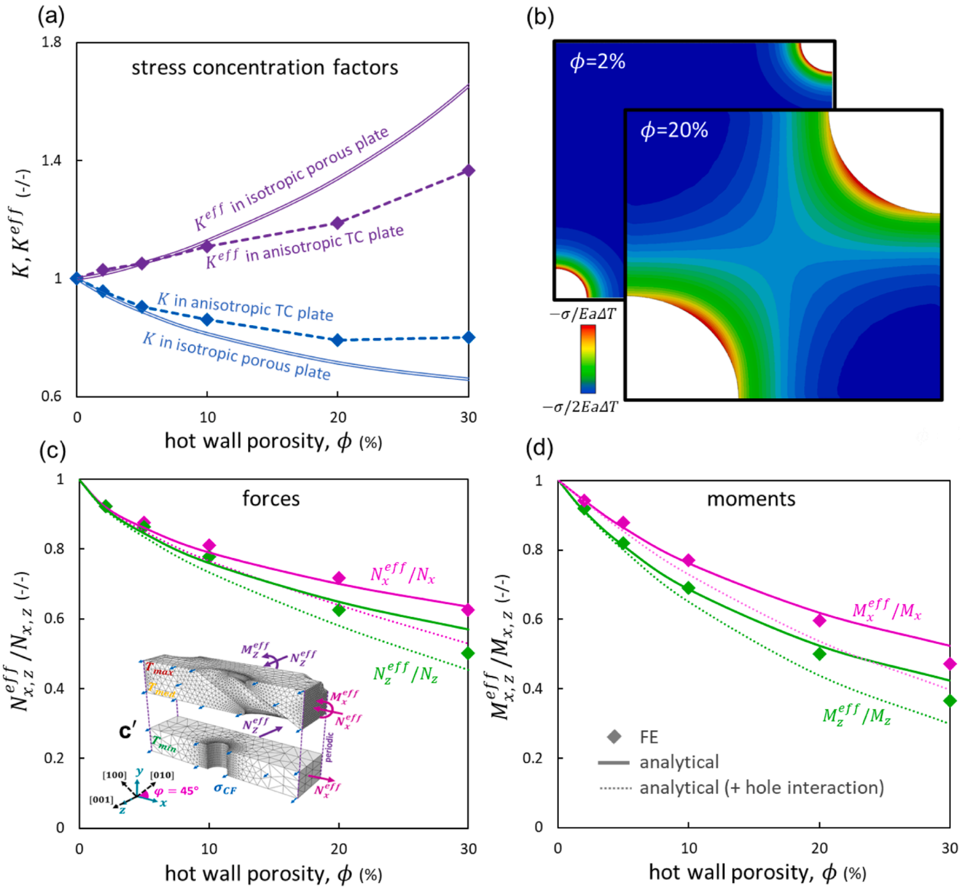

Fig. 5. Investigation of porosity effects. **a** variation of bulk stress concentration factor K and effective stress concentration factor K^{eff} with porosity Φ for the 2D isotropic plate in Fig. 5b and the transpiration cooling system of Fig. 3c2 (also shown in the inset Fig. 5c'). **b** normalised maximum principal stress field in FE models for circular holes in 2D isotropic plates constrained at their ends and experiencing uniform temperature; the low porosity Φ=2 % approximates the isolated hole in an infinite plate solution where stresses are uniform along the hole edge; the case Φ=20 % leads to non-uniform stresses along the hole edge and therefore higher K^{eff} despite the hole–hole interaction. **c-d** reduction of effective (volume averaged) axial forces and bending moments in the model of Fig. 5c' with porosity, in terms of the ratio of effective value in the presence of holes over the fixed bulk value in the absence of holes; FE calculations are compared against the analytical model for 2D orthotropic porous plates (with and without hole interactions) developed in [52,53].

the key output of the LOM.

3.1. Local plastic-creep deformation

The utility and importance of the peak elastic stress σ* can be explained based on the true cyclic inelastic stress-strain response shown in Fig. 6a for 20 subsequent load cycles, obtained by full CPFE analysis of the system in Fig. 3c2 under the cyclic thermal-centrifugal load history shown in the inset Fig. 6c1 with temperature field parameters at full loading T_{max}=845 °C, ΔT=90 °C, $\overline{\Delta T}_h$=0.47 (corresponding to input parameters T_∞=1700 °C, $\dot{m}^*$=6, ϕ=10 %) and by using the full elastic–plastic-creep parameters calibrated for the CMSX-4 Nickel superalloy summarised in Table 2. Fig. 6b shows the corresponding inelastic stress–strain response for five subsequent load cycles when the temperature field parameters are augmented to T_{max}=866 °C, ΔT=106 °C, $\overline{\Delta T}_h$=0.47 (corresponding to input parameters T_∞=2100, $\dot{m}^*$=6, ϕ=10%). A description of the CPFE analysis is given here in Appendix C, with further details provided by the authors in [22]. Here we examine firstly the resulting inelastic stress-strain response in Fig. 6a which involves the following sequence of events:

A. Material yielding in compression to state A on 1st engine start-up – the stress here decreases due to the reduction of yield stress with temperature, i.e. the stress at state A is equal to the yield stress at maximum temperature $\sigma_{y_{T_{max}}}$.
B. Stress relaxation to state B due to creep strain generated during steady-state operation at the peak temperature T_{max}, known as 'creep dwell'.
C. Elastic unloading by the amount S^* to the residual stress ρ^T (state C) upon 1st shutdown.
D. Elastic re-loading by the amount S^* to state D upon 2nd start-up, which coincides with point B.
E. subsequent creep deformation and stress relaxation to state E.

The behaviour for a higher thermal load shown in Fig. 6b displays similar features with the difference that upon 1st shutdown the residual stress ρ^T reaches the room temperature yield stress σ_{y_R} (dashed pink line) and therefore plasticity occurs between states C and C'; in this case reloading from state C' leads to state D followed creep and stress relaxation to point E during steady state operation. Here point E approximately coincides with B, i.e. each subsequent creep dwell leads to the same stress at the end of dwell such that the strain-stress cycle can be practically considered stabilised, known as plastic shakedown i.e. only small changes occur with subsequent cycling due to some ratchetting effects observed in Fig. 6b.

In contrast to the virtually stable response of Fig. 6b, the case of Fig. 6a displays a transient behaviour with the sequence A-B-C-D-E continuing with further cycling; here the amount of stress relaxation for each subsequent cycle decreases due to the dependence of creep rate on current stress, i.e. no more creep would occur if the stress during

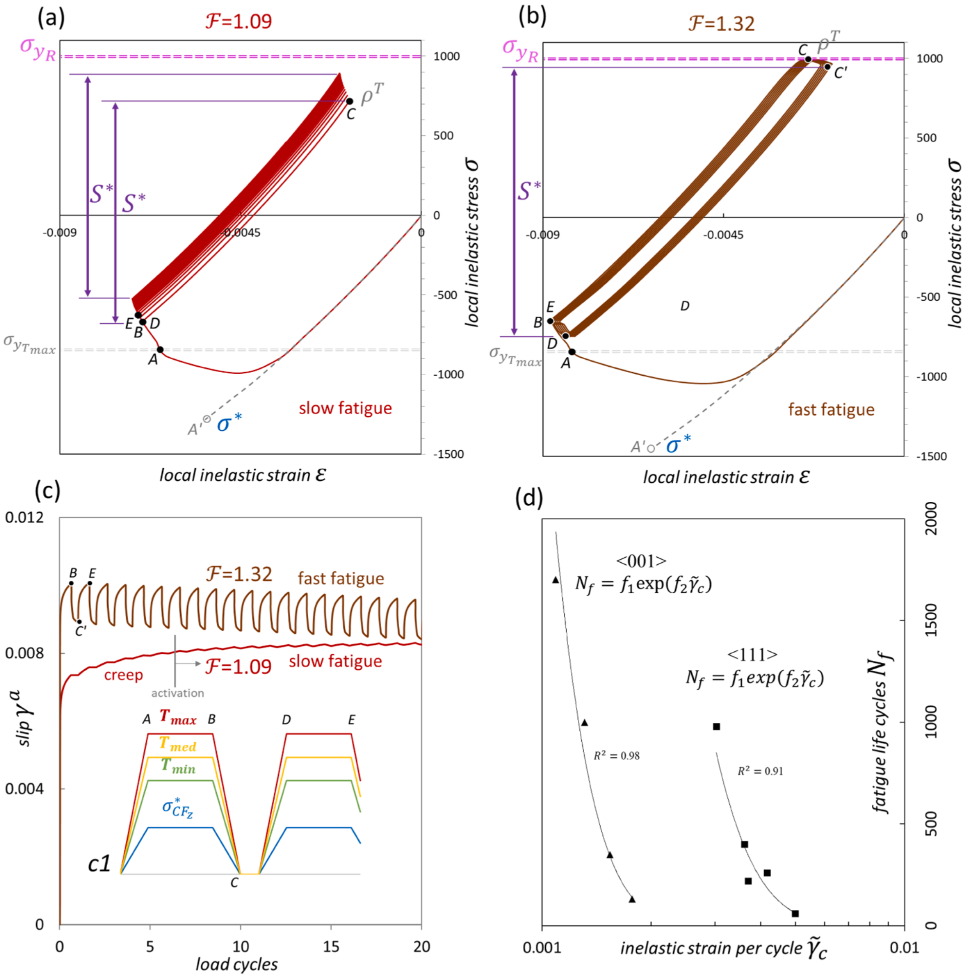

Fig. 6. Local inelastic behaviour and fatigue assessment for the film cooling hole of Fig. 3c2. **a-b** cyclic stress–strain responses for low thermal loading and high thermal loading, predicted by applying the thermal load history in Fig. 6c1 in the CPFE model of Fig. 3c2 for 20 cycles; we plot maximum absolute principal stress and the strain along the current direction this stress. Dashed line ending at point A' denotes the fictitious elastic stress σ*; S^* denotes the cyclic stress range; σ_{y_R}, $\sigma_{y_{T_{max}}}$ are the yield stresses at room temperature and peak temperature of the thermal cycle. **c** history of plastic slip in the most active slip system for the cases of Fig. 6a and b; inset 6c1 shows the type of thermomechanical load cycles used in the study. **d** fatigue life model construction by fitting low cycle fatigue data for CMSX-4 Nickel alloy [55]; the inelastic strain per cycle is expressed in terms of the slip accumulation per cycle $\tilde{\gamma}_c$ and N_f are the load cycles required for fatigue crack initiation.

operation relaxed to zero (known as ‘elastic shakedown’). The latter, however, can only occur if the residual stress ρ^T (C point of every cycle) never reaches the room temperature yield stress σ_{y_R} (dashed pink line) otherwise plastic deformation will occur on engine shutdown like in Fig. 6b. If the latter happens then the behaviour will switch from the pure ‘creep’ regime to the ‘low cycle fatigue’ regime, here referred to as simply ‘fatigue’. In fact, this switch from the creep regime to the fatigue regime does occur in the case of Fig. 6a after a small number of cycles, but this is not directly evident in the figure due to ρ^T being smaller than σ_{y_R} even after the 20 cycles shown; we note here that room temperature plasticity begins to occur even when stresses approach the yield stress due to the full rate dependent plasticity of CMSX-4 being modelled (see Appendix C). The switch from creep to fatigue for the case of Fig. 6a can be identified by the cyclic plastic slip γ^a reversals shown in Fig. 6c for the most active crystallographic slip system, i.e. once fatigue is activated γ^a starts to vary cyclically around a mean value. Since the amplitude of these reversals is small for the case of Fig. 6a, this is referred to as ‘slow’ fatigue, whereas the severe cyclic γ^a amplitudes shown in Fig. 6c for the case of Fig. 6b imply that the latter is a case of ‘fast’ fatigue with low fatigue crack initiation life expectancy.

In general, whether or not a critical stress raiser will operate in the fatigue regime after a number of cycles can be predicted by comparing the unloading/re-loading stress amount S^* against the room temperature yield stress σ_{y_R}. If $S^*\leq\sigma_{y_R}$ then the pure creep regime prevails - if instead $S^*>\sigma_{y_R}$ then fatigue will be activated at some stage during the cyclic loading history. We can now define the index $\mathcal{F}= S^*/\sigma_{y_R}$ such that $\mathcal{F}>1$ indicates that fatigue will occur after an initial number of cycles, followed by additional cycles N_f until a crack initiates, and $\mathcal{F}\leq 1$ indicates that only creep strain is encountered, effectively during the steady-state high temperature operation period of each successive load cycle.

3.2. Enhancement of residual stresses due to temperature dependent elasticity

It becomes paramount to determine S^* without the need to run CPFE simulations but instead derive it based on the elastic peak stress σ* at full loading which is readily obtained from the stress code of LOM (known as elastic fictitious stress range).

As shown in Fig. 6a, the unloading/re-loading stress amount S^*, also here referred to as ‘actual cyclic stress range’, and the absolute stress $|\sigma_B|$ at the end of each creep dwell (state B), together define the residual stress ρ^T on shutdown as $\rho^T = S^* - |\sigma_B|$, where the superscript T denotes that the full temperature dependence of elastic constants (Fig. 2a) is considered. In principle, residual stresses scale with a) the amount of inelastic strain generated during loading and steady state operation, and

Table 2

Summary of elastic-plastic-creep parameters used for the CMSX-4 Nickel superalloy in the CPFE analysis and subsequent fatigue-creep life assessment results of Fig. 8d. The stress code of the LOM uses only the elastic parameters and the room temperature yield stress.

Elasticity	Notation	Value
elastic constants	C_{11}, C_{12}, C_{44}	Fig. 2a
thermal expansion coefficient	α	Fig. 2a
plasticity	$\dot{\gamma}_0$	$7.07x10^{-5}/s$
reference slip rate	$\dot{\gamma}_0$	$7.07x10^{-5}/s$
coefficient of the power function $m(T)$	m_1	– 0.036/ K
constant of the power function $m(T)$	m_2	65.34
critical resolved shear stress (CRSS) for octahedral slip	τ_c^{oct}	Fig. 2b
critical resolved shear stress (CRSS) for cubic slip	τ_c^{cube}	Fig. 2b
creep (initial creep rate $\dot{\mathscr{S}}$)		
reference rate for initial creep	$\dot{\mathscr{S}}'_o$	$2x10^7/s$
stress sensitivity factor for initial creep	$\mathscr{S}'_\sigma$	$5x10^{-2}$/ MPa
activation energy for initial creep	$Q_{\mathscr{S}}$	$440x10^3$J
controls the reduction of $\dot{\mathscr{S}}_o$ at high T **(rafting/ creep strengthening)**	$w_{\dot{\mathscr{S}}_o}$	22
temperature beyond which $\dot{\mathscr{S}}_o$ reduces with T	$T_{\dot{\mathscr{S}}_o}$	1213 K
controls the increase of the dependence of $\dot{\mathscr{S}}$ on stress with increasing T	$w_{\mathscr{S}_\sigma}$	5
temperature beyond which the above stress dependence increases with T	$T_{\mathscr{S}_\sigma}$	1173 K
creep (damage/strain softening coefficient Ω)		
reference rate for creep damage/strain softening	Ω'_o	$3x10^{-1}/s$
stress sensitivity factor for creep damage/strain softening	Ω_σ	$3.5x10^{-2}$/ MPa
activation energy for creep damage/strain softening	Q_Ω	$440x10^3$ J
controls the reduction of Ω_o at low T **(primary-tertiary creep transition)**	w_{Ω_o}	15
temperature below which Ω_o reduces with decreasing T	T_{Ω_o}	1203 K

b) the elastic constants (Young's modulus), since these govern the compatibility of strains which must be always satisfied in any structure. It can be shown based on Fig. 2a that the Young's modulus of the CMSX-4 Nickel alloy in the crystal directions ⟨001⟩, ⟨110⟩, ⟨111⟩ respectively increases by a factor of 1.77, 1.6 and 1.43 upon shutdown from a high temperature operation 1100 °C to room temperature 20 °C. This in principle implies that the residual stresses at the shutdown state are severely enhanced by the temperature dependence of Young's modulus. If this dependence is ignored, e.g. if the high temperature Young's modulus is used throughout the structure, then the residual stresses will be erroneously predicted significantly lower.

For the hypothetical case of constant modulus, it can be shown that the residual stresses ρ on shutdown can be very accurately approximated as $\rho = \sigma^* - |\sigma_B|$, which implies that the elastic fictitious/peak stress at full loading σ^* would also be the actual cyclic stress range. In fact, this is consistent with all studies published to date under the assumption of constant Young's modulus (i.e. modulus which does not vary throughout the loading cycle) including the widely used Neuber/Glinka schemes [56,57] and shakedown/ratchetting solutions [58–60]. Further analysis here has also verified that the stress at the end of the creep dwell σ_B does not change between using the true full temperature-time variation of Young's moduli and using a constant modulus, provided that in the latter case the moduli corresponding to the temperature field at full loading are considered (modulus varies in space throughout the structure but not in time). The reader is referred to a complementary study by the authors in [61] for a detailed comparison between the cases of varying and constant modulus in a simplified two-plate system.

By simply dividing the above ρ^T and ρ expressions we can now relate S^* to σ^* through:

$$S^* = |\sigma_B| + \widehat{\rho}\ (\sigma^* - |\sigma_B|) \tag{1}$$

where $\widehat{\rho} = \rho^T/\rho$ is the residual stress enhancement factor associated with the temperature dependence of Young's modulus. In the limiting case where the stress relaxes to zero at full loading, i.e. $|\sigma_B| = 0$ (which is only considered here to assess whether or not fatigue will occur – Section 3.1) we then have $S^* = \widehat{\rho}\ \sigma^*$ and the fatigue index can be finally written as:

$$\mathscr{F} = \frac{\widehat{\rho}\ \sigma^*}{\sigma_{y_R}} \tag{2}$$

Evidently, if $\widehat{\rho}$ is known then one can predict whether fatigue will occur based on the elastic stress code of the LOM. Exact determination of $\widehat{\rho}$ requires full CPFE analysis of at least one load-unload cycle. Conservatively, nevertheless, we can consider the upper bound of $\widehat{\rho}$ corresponding to the vicinity of a stress raiser, which is simply the ratio between the Young's modulus E_o at room temperature (shutdown sate) and the Young's modulus E_T at the local peak temperature T (fully loaded state). Fig. 7 summarises our results surrounding the value of $\widehat{\rho}$ for the critical direction ⟨111⟩ along which the peak stresses apply at the film hole under pure thermal loading and the worst case of crystal-plate misalignment angle of 45° as shown in Fig. 3c1; the inset Fig. 7 plots the upper bound E_o/E_T for each peak temperature T, computed based on the elastic constants of Nickel in Fig. 2a – the upper bounds at the two distinct peak temperatures T=900 °C and T=1100 °C then provide the horizontal dashed lines in Fig. 7, which are compared against actual $\widehat{\rho}$ values determined from full cyclic CPFE simulations with varying thermal difference ΔT at full loading in the range 50–400 °C across the TC system in Fig. 3c2 and maximum temperatures T_{max} = 900 °C and T_{max}=1100 °C.

Our interpretation of Fig. 7 and underlying CPFE results is as follows. As ΔT decreases the accumulated plastic-creep strain field in the TC structure becomes more localised to the film hole region, i.e. the vicinity of the stress raiser about which is the analysis is performed, and as such, the $\widehat{\rho}$ value approaches the upper bound, i.e. becomes independent of non-local effects. Inversely, an increasing ΔT increases the non-locality

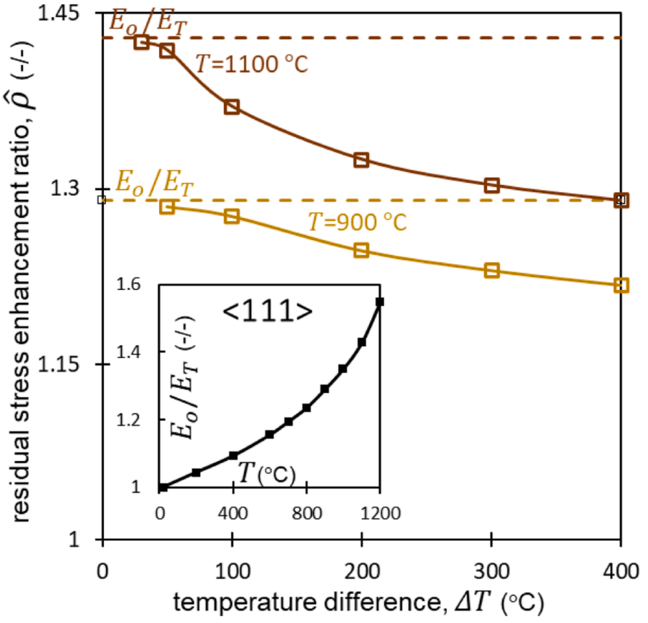

Fig. 7. Variation of the residual stress enhancement ratio $\widehat{\rho}$, associated with the temperature dependence of Young's modulus, with the total thermal difference ΔT and maximum temperature T_{max} in the TC system of Fig. 3c2; results obtained by full CPFE analysis. Dashed lines represent the upper bound values of $\widehat{\rho}$ equivalent to the ratio of room temperature to high temperature Young's modulus E_o/E_T. Inset figure shows the variation of E_o/E_T across the full peak temperature range.

of plastic and especially creep deformation within the structure, and this additional interaction of the critical location with the surrounding plastic-creep volume serves to reduce $\widehat{\rho}$; this is consistent with the fact that $\widehat{\rho}$ reduces with ΔT much more for T_{max}=1100 °C than for T_{max}=900 °C, as in the former case the non-local creep deformation within the hot wall is much more severe.

Practically, the TC system here is being designed for operation in the range T_{max}=900–1000 °C and $\Delta T < 150$ °C, for which the upper bounds E_o/E_T provide a conservative and yet reasonably accurate estimation. This eventually indicates that the fatigue index $\mathscr{F}$ can be reliably calculated based on the elastic stress code of the LOM.

3.3. Fatigue index $\mathscr{F}$ diagrams

The fatigue and creep regimes of behaviour at the critical location of the film hole are displayed in the output design diagram of the LOM in Fig. 3e, as well as the more detailed diagrams in Fig. 8. Pure creep failure at film cooling holes in the $\mathscr{F}\leq 1$ regime is unlikely for the type of TC systems considered here, because the displacement controlled compressive thermal stresses at the outer hot wall surface dominate over any existing force controlled tensile centrifugal stresses, and therefore creep at high temperature involves significant stress relaxation to stress levels which are too low for the associated creep rates to be critical for failure, i.e., the creep rates are low enough such that the total creep strain accumulated after a large number of service cycles is still much lower than the creep rupture strain of Nickel superalloys [49]. Hence, in this paper we focus on the detrimental situation of low cycle fatigue failure driven by severe thermal stresses, often called ‘fatigue-creep failure’ or failure due to ‘fatigue-creep interaction’ in the sense that creep at high temperature enhances plasticity at low temperature and vice versa [22].

By following the LOM workflow in Fig. 3 for the elastic-thermal and room temperature yield properties of Nickel superalloys (Fig. 2a an b) and by using four different combinations of input parameters from Table 1, we now produce Fig. 8a–d which show the variation of the $\mathscr{F}$ index at the critical film cooling hole location with respect to porosity Φ and hot gas temperature T_∞ for each of these four cases. In all cases, as T_∞ increases we must use a higher Φ to avoid fatigue, i.e. $\mathscr{F}<1$. Extremely high ϕ values of 20 % are required to avoid fatigue in the case of Fig. 8a, which corresponds to pure thermal loading and a minimum coolant flow rate $\dot{m}^*$=3. These critical Φ values, however, reduce dramatically when $\dot{m}^*$=6 in Fig. 8b and even further when also an inner wall 50 % thinner than the outer wall is used in Fig. 8c, and even further when thermal loading is also combined with a centrifugal load of 200 MPa (Fig. 8d).

The benefit of higher $\dot{m}^*$ (Fig. 8b) owes to a decreasing bulk thermal stress $\sigma^*_{o_x}$ driven by the reduction of maximum temperature T_{max} and thermal difference ΔT with $\dot{m}^*$ as shown earlier in Fig. 3b1-b2. The benefit of reducing inner wall thickness (Fig. 8c) owes again to a decreasing $\sigma^*_{o_x}$, but this now relates solely to the isostrain wall condition becoming less constricting as the inner wall gets thinner. Lastly, the benefit of centrifugal loading (Fig (8d) is underpinned by the reduction

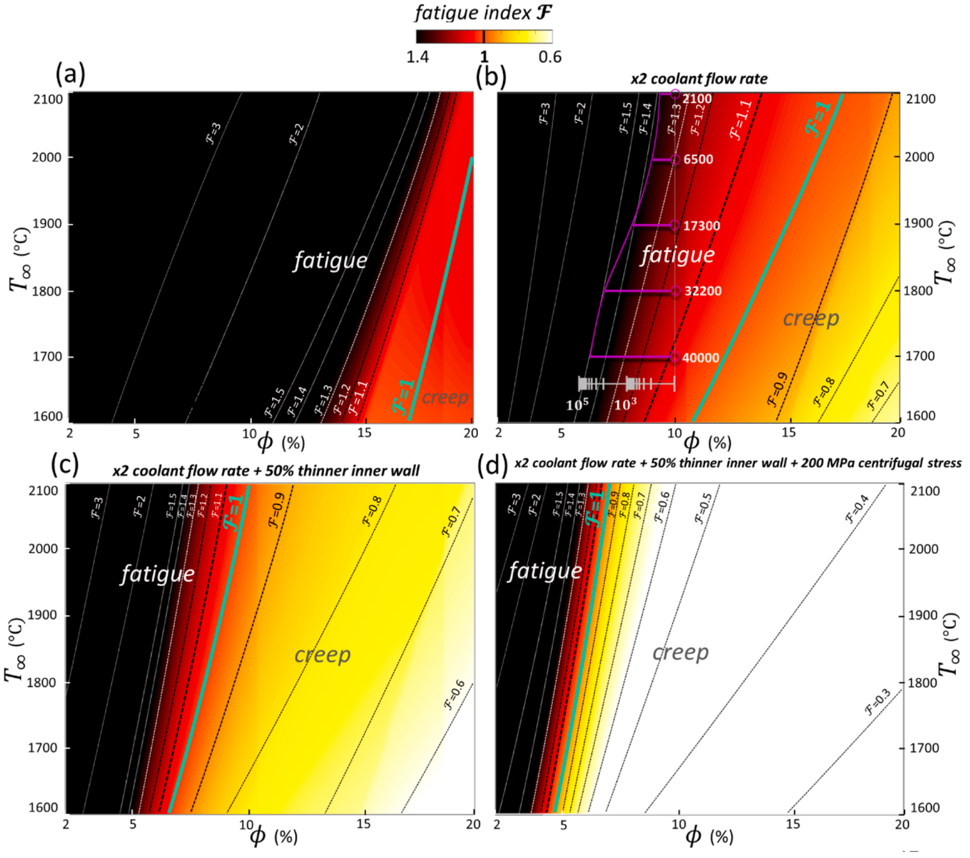

Fig. 8. Design diagrams produced ‘rapidly’ by the low order aerothermal-stress model (LOM) of Fig. 3, showing fatigue index $\mathscr{F}$ contours for the critical film hole location as a function of hot gas temperature T_∞ and outer wall porosity Φ; **a** worst fatigue scenario of pure thermal loading with coolant mas flow $\dot{m}^*$=3. **b** improved fatigue scenario when the coolant flow is doubled. **c** further improved scenario when the inner wall is 50 % thinner than the outer wall. **d.** maximum improvement when also a net centrifugal stress of $\sigma^*_{CF_z}$ = 200 MPa is applied in-phase with the thermal loading. $\mathscr{F}=\widehat{\rho}\ \sigma^*_{o_x}K/\sigma_{y_R}$ is calculated as the ratio of augmented elastic stress $\sigma^*=\widehat{\rho}\ \sigma^*_{o_x}K$ (calculated by the LOM in Fig. 3) and room temperature yield stress σ_{y_R}=1100 MPa of the CMSX-4 Nickel superalloy (averaged over ⟨001⟩,<011>,<111> orientations [22]). Fatigue life results from CPFE simulations of the model in Fig. 3c2 are also shown in Fig. 8b: the cyclic slip per cycle (Fig. 6c) is used to predict the number of service cycles N_f required for fatigue crack initiation (based Fig. 6d).

of stress concentration factor K with the loading ratio $\lambda_{CF/T}$ shown earlier in Fig. 3d2; note however that our analysis here assumes that thermal and centrifugal loading cycle in-phase. In summary, Fig. 8 shows that if favourable conditions are combined then fatigue can be substantially suppressed.

3.4. *Crystal plasticity-based fatigue life assessment*

To validate the fatigue index diagrams in Fig. 8, we perform CPFE simulations for particular cases in the wide range $1700\,^{\circ}\mathrm{C} < T_{\infty} < 2100\,^{\circ}\mathrm{C}$ and fixed $\dot{m}^{*}=6$, $\Phi=10\%$, for which fatigue is predicted to operate in Fig. 8b; we predict the inelastic response of the system in Fig. 3d2 over 50 consecutive pure thermal cycles of the type shown in the inset Fig. 6c1 and use the inelastic strain $\tilde{\gamma}_c$ accumulated over the last cycle at the critical film hole location to predict the fatigue crack initiation cycles N_f based on our proposed fatigue life assessment model in Fig. 6d; the latter is described and justified in Appendix D. We should mention here that for the worst case scenario of crystal-wall misalignment considered through the study (see Fig. 3c1-c2) the maximum absolute principal stress at the critical location of the film hole always applies locally along the <111> crystal direction under pure thermal loading; for example, we have verified that the current stress-strain slopes at each temperature during the initial elastic regimes of the first start-up in Fig. 6a and b are consistent with the current Young's modulus along $\langle 111 \rangle$ at each corresponding temperature (which also indicates that the stress state at the hole is strongly uniaxial). The above imply that cubic slip systems dictate the inelastic response, and as such, all the fatigue life cycles calculated in Fig. 8b refer to the fatigue life model calibrated for cubic slip in Fig. 6d; more details on the alignment of local principal stress with the crystal axes are available in [22].

The case of $T_{\infty}=1700\,^{\circ}\mathrm{C}$, $\dot{m}^{*}=6$, $\phi=10\%$ lies just above the $\mathscr{F}=1$ boundary, i.e. $\mathscr{F}=1.09$ (Fig. 8b) and corresponds to the scenario of slow fatigue in Fig. 6a discussed earlier; for this case we predict $N_f=40{,}000$ which is consistent with the characterisation 'slow fatigue' that was used so far, in the sense that 40,000 cycles can be considered a large number in the context of low cycle fatigue. On the other hand, the case of $T_{\infty}=2100\,^{\circ}\mathrm{C}$, $\dot{m}^{*}=6$, $\phi=10\%$ falls at the upper bound of the diagram in Fig. 8b, i.e. $\mathscr{F}=1.32$ (Fig. 8b) and corresponds to the scenario of fast fatigue in Fig. 6b; for this case we predict $N_f=2100$ which again is consistent with our qualitative predictions that this scenario leads to crack initiation within a low number of cycles. All the above add validity to our diagrams produced via the LOM. Turbine blades are typically designed for a service life of 10^4 cycles [21], indicating that a fatigue index up to $\mathscr{F}=1.2$ can be reliably considered satisfactory based on Fig. 8b. However, further increase in $\mathscr{F}$ (or equivalently in T_{∞}) in Fig. 8b reduces our N_f predictions exponentially and leads to unsatisfactory performance.

4. Discussion

We now provide an evaluation of our newly developed methods and results in the context of the challenges that currently underpin the design and commercialisation of transpiration cooling (TC) systems.

4.1. *Challenges of transpiration cooling (TC) systems*

Our study here confirms our earlier work [22] to strongly indicate that inappropriate design of TC systems leads to extreme plastic-creep deformation at film cooling holes and quick fatigue failure within a very low number of service cycles. We have explored these implications for double wall TC systems made of single crystal Nickel superalloys where the following four detrimental effects synergistically apply: A. severe bulk thermal stresses due to the temperature mismatch between the hot/outer and cold/inner wall, B. misalignment between the principal crystal axes and wall axes along which the bulk thermal stresses apply, C. severe local stress concentration at film cooling holes, and D. significant enhancement of residual stresses due to the temperature dependence of Young's modulus. While B-D effects are relevant to any type of single crystal curved component where cooling holes with large inclination are used, the A effect is specific to double wall systems. Single wall components will not experience the membrane thermal stresses generated here by a combination of wall temperature mismatch and kinematic wall coupling [17]. They will only experience bending thermal stresses (along with centrifugal σ_{CF} stresses), which suggests that tensile stress states at inclined film cooling holes could dominate during high temperature plasticity-creep and the inner rim of these holes will be more critical as σ_{CF} increases compared to the outer hotter rim investigated here. The presence of tensile thermal stresses in this case may change the significance of creep versus low cycle fatigue in single wall systems. This can be readily investigated using the low order aerothermal-stress model (LOM) developed in this paper, since the case of a single wall TC system is a special case of the more general and complex problem of the double wall TC system geometry considered here; this immediately creates an avenue for future research not only in the field of turbomachinery but also hypersonic transport. With regards to the severity of stress concentration at film cooling holes and related mitigation strategies, the reader is referred to our relevant work in [22]. Lastly, the crucial effect of residual stress enhancement identified here for the first time, points towards the need to reduce the maximum wall temperature as much as possible, since this controls the amount by which Young's modulus and therefore residual stresses increase on gas turbine shutdown. Residual stresses, in turn, control the severity of plasticity on shutdown and therefore the severity of plastic slip reversals upon cycling loading, hence the severity of low cycle fatigue damage and failure. Again, our work here lays the foundation for a more elaborate investigation of the effect of residual stress enhancement by the temperature dependence of Young's modulus in cyclic thermomechanical loading problems – this concerns not only the creep-fatigue of core gas turbine components and hypersonic systems, but also potentially the creep-fatigue of fusion first wall Tungsten-steel joints [62,63] and the delayed hydride cracking of Zircaloy fission fuel cladding [64].

4.2. *Benefits of transpiration cooling (TC) systems*

A key conclusion here is that dense arrays of film cooling holes enhance both the cooling and the mechanical performance, which provides an opportunity to achieve a step change in the overall performance of future high temperature components. Our results demonstrate that future turbine blades that employ transpiration cooling with many impingement and cooling holes will be able to operate in higher environmental temperatures than conventional blades, whilst generating higher temperature differentials within the blade, with the resulting thermal stresses limited by the low effective stiffness arising from the high hole density. The synergy of these benefits could eventually allow turbine blades to operate under gas temperatures in excess of 2000 °C, whilst satisfying the fatigue-creep performance requirements. The amount of coolant required to feed the cooling holes in designs of this type has been a longstanding concern of the community, which we have addressed in the development of our new coupled aerothermal-stress design approach.

4.3. *Merits of the low order aerothermal-stress model (LOM)*

Beyond predicting solid-fluid interactions and fatigue-creep behaviour under particular engine conditions, we place emphasis here on creating a framework that captures the interactions between gas turbine operation, geometric parameters, cooling performance and structural integrity. The newly developed LOM allows the designer to rapidly: a) assess whether a TC aerofoil will survive under a given set of conditions; b) tune parameters to balance cooling and mechanical performance; and c) identify the limited number of critical situations for which expensive

CFD/CPFE simulations are needed. Consequently, amongst a number of crucial effects revealed here with regards to the density of cooling holes, the gas turbine temperature and the thermal-centrifugal loading history, the LOM also provides us with a rapid calculation of the amount of coolant required to achieve the design temperatures and its direct impact on thermal stresses and fatigue performance. Reducing coolant consumption is key to minimising aerodynamic losses caused when coolant is ejected into the mainstream flow, and to maximising flow rates for combustion, as a loss of 5% of air for cooling results in a 1% penalty in the fuel burn [65]. The cost-effective nature of the aerothermal-stress calculations of the LOM encourages its further use towards quantifying the role of internal cooling characteristics, such as the density/size of the pedestals connecting the two walls of twin-wall TC components, as well as the role of external cooling characteristics, such as the film cooling hole size and shape. It provides a basis which can be extended to exploit new opportunities for multi-level component optimisation. For instance, aerofoils with variable hole density could be designed in high heat flux regions, whilst minimising coolant waste in low flux regions alongside minimising the danger of hot gas ingestion [9, 24].

4.4. The aspect of yield stress anisotropy

The simplicity and speed by which the LOM produces the design diagrams of Fig. 8 is mainly associated to the conservative nature of our fatigue life assessment and partially to the clever idealisations used in the heat transfer-stress computations. The key purpose of the LOM is to provide the boundary beyond which low cycle fatigue failure operates in a critical location, or equivalently, to provide us with combinations of conditions under which fatigue failure does not occur within the design life. The fatigue boundary is found by simply comparing the yield stress σ_{y_R} of the material at room temperature with the residual stress generated at the critical location upon engine shutdown, which correlates with the local elastic stress determined from a straightforward elastic analysis. It is important to note that the magnitude of the yield stress σ_{y_R} in single crystal turbine blade components is generally anisotropic and depends on the local stress direction, which in turn depends on a range of parameters at critical locations, such as film cooling holes, which includes: the relative magnitudes of the centrifugal-thermal loads [22]; the blade wall-crystal misalignment [9,22]; and the hole geometry. This may not be a limiting factor when calculating the fatigue boundary in Nickel superalloys where σ_{y_R} is weakly anisotropic [22], but it may be a concern for other alloys. Therefore, future work is encouraged to explore the merits of LOM in a range of high temperature materials. Further work may also investigate the degree by which the elastic, plastic and creep material anisotropy can be used to advantage within design; for example, one can explore potential benefits from optimising the film hole shape such that the local stress aligns with the crystallographic direction where the yield stress maximises and/or creep rate minimises [22].

4.5. The conservatism of life assessment

This may not be a limiting factor when calculating the fatigue boundary in Nickel superalloys where σ_{y_R} is weakly anisotropic [22], but it may be a concern for other alloys. Therefore, future work is encouraged to explore the merits of LOM in a range of high temperature materials. Further work may also investigate the degree by which the elastic, plastic and creep material anisotropy can be used to advantage within design; for example, one can explore potential benefits from optimising the film hole shape such that the local stress aligns with the crystallographic direction where the yield stress maximises and/or creep rate minimises [22].

Once we enter the regime above the fatigue boundary, we then need to look at how many cycles N_f it takes for fatigue crack initiation to occur in order to reject designs for which N_f is too low. The number of material and load parameters that now come into play increases immensely, to the extent that it becomes very difficult to relate N_f to the thermo-mechanical load history in a pseudo-analytical manner, as employed in the LOM. Our CPFE simulations in Fig. 8b show that elevations of thermal loading (or the fatigue index $\mathscr{F}$) can reduce N_f to unacceptable values, which is largely due to the high creep rate of Nickel at very high temperatures combined with the long steady-state periods (creep dwells) of three hours considered in this study. Shaping holes to manipulate the local stress direction in this regime requires full consideration and accurate modelling of both material creep and yield anisotropy, as well as creep/yield tension-compression asymmetry which remains a challenge [22,66,67].

A final consideration is that even when we look at fatigue crack initiation, a strong degree of conservatism typically remains since the local strain approach used in Fig. 8b and the underpinning fatigue life model in Fig. 6d (described in Appendix D) ignores non-local effects and does not take into account the time for a nucleated crack to subsequently propagate through the structure leading to ultimate failure. Furthermore, crack initiation can be sensitive to the volume of material experiencing the high stress level, while crack propagation, which is completely ignored here, can make an important contribution to final component life [68–70]. Densely packed holes can act as crack arrest sites [34,36,37], such that fatigue failure is potentially benign; also changes in surface chemistry morphology from exposure to atmospheric contaminants will affect all the above [71,72]. Catastrophic failure predictions underpinned by all these aspects relies largely on costly and time-consuming experiments [73]. As with expensive CFD/FE simulations, the design diagrams described here can also guide the experimental studies by quickly identifying the most meaningful sets of conditions to employ in any programme of tests.

5. Conclusions

We have developed a low order mass-heat transfer-stress model (LOM) which rapidly evaluates the coupled aerothermal-mechanical performance of complex double wall Transpiration Cooling (TC) systems and provides a firm quantitative basis for introducing TC systems in gas turbines and hypersonic vehicles.

The simplicity and computational speed of the mass-heat transfer calculations of the LOM owes to the discretisation of complex TC geometries into networks of one-dimensional (1D) mass-heat elements which can be readily solved by iterative Newton-based methods. The simplicity-efficiency of stress calculations of the LOM owes to the use of analytical solutions for thermally loaded anisotropic plates, the initial assumption of a purely elastic material response, as well as the knowledge of how stresses intensify at stress raisers and by how much residual stresses increase due to the temperature dependence of Young's modulus. Within seconds, the LOM indicates whether the detrimental low cycle fatigue (LCF) failure process will be activated after a number of service cycles at a critical location of a TC system.

This provides quick answers to conceptual/preliminary design questions, allowing the designer to adjust the coolant flow rate, the density of film cooling holes, and the hot gas (turbine inlet) temperature towards mitigating LCF failure, without needing to perform expensive (Computational Fluid Dynamics) and/or Crystal Plasticity Finite Element (CPFE) simulations. Simultaneously, the LOM rapidly identifies the particular-critical situations where LCF failure operates, for which detailed CFD and/or CPFE analyses are typically performed to finalise and/or qualify the design. We believe that our proposed scheme for estimating the enhancement of residual stresses at a stress raiser due to the temperature dependence of Young's modulus should be considered in any study of thermomechanical fatigue.

We find that double wall transpiration cooled single crystal Nickel turbine blades can exhibit unacceptable LCF life if design is inadequate, but LCF is suppressed if a large enough density of film cooling holes is used. This previously unexplored benefit of film holes owes to the threefold reduction of metal temperatures, temperature gradients and blade wall stiffness as the outer wall porosity increases.

Our work encourages the adoption of the LOM in current industrial design practises and the implementation of TC systems in high temperature applications. The coupled aerothermal-structural LOM framework was developed in conjunction with Rolls-Royce plc to accelerate preliminary design studies for double wall systems. The LOM has been validated against results from industrial standard conjugate models and experimental data for designs of direct relevance to future high pressure turbine blades and vanes.

CRediT authorship contribution statement

Christos Skamniotis: Writing – original draft, Validation, Software, Methodology, Investigation, Formal analysis, Conceptualization. **Michael van de Noort:** Writing – review & editing, Software, Investigation, Data curation, Conceptualization. **Alan C.F. Cocks:** Writing – review & editing, Funding acquisition. **Peter Ireland:** Supervision, Project administration, Funding acquisition.

Declaration of competing interest

The authors declare the following financial interests/personal relationships which may be considered as potential competing interests:

Peter Ireland reports financial support was provided by Engineering and Physical Sciences Research Council. Peter Ireland reports financial support was provided by Rolls-Royce plc. If there are other authors, they declare that they have no known competing financial interests or personal relationships that could have appeared to influence the work reported in this paper.

Acknowledgements

This research was supported by the EPSRC programme grant EP/P000878/1 and funding from Rolls-Royce PLC.

Appendix

A. Details of aerothermal calculations of the LOM

The aerothermal calculations underpinned by Fig. 4a assume an irreversible, steady and incompressible coolant mass flow which is discretised into five 1D flow elements as follows: 1) impingement hole flow, 2) flow associated with cavity expansion and impingement on the outer wall, 3) flow associated with acceleration away from stagnation point, 4) flow around pedestal, and 5) film cooling hole flow.

Mass flow through a 1D element with inlet node i and outlet node j is determined by the pressure difference P_i - P_j, the density ρ_i, and the effective compliance of the element to the mass flow $C_{i,j}$ found from an empirical correlation (e.g. discharge coefficient equation for impingement and film hole flows). If a node j is connected to n inlet nodes i and m outlet nodes k, the mass flow is determined by solving for continuity at each node j using:

$$\sum_i^n \dot{m}_{i,j} - \sum_k^m \dot{m}_{j,k} = \sum_i^n \mathrm{C}_{i,j}\sqrt{\rho_i}\sqrt{P_i - P_j} - \sum_k^m \mathrm{C}_{j,k}\sqrt{\rho_j}\sqrt{P_j - P_k} = 0 \tag{A1}$$

In order to form the energy flow network in Fig. 4a, seven forms of convective heat transfer are considered using 1D energy flow elements, as follows: 1) external heat transfer to the external surface of the hot wall from the mainstream gas, 2) impingement cooling at the inner surface of the hot wall, 3) additional cooling at the inner surface of the hot wall due to radial wall jets, 4) in-hole film cooling, 5) cooling at the inner surface of the cold wall, 6) in-hole impingement cooling, and 7) natural convection to the coolant plenum from the external surface of the cold wall.

Empirical correlations from the literature are also used to determine fluid mass flows and heat transfers of internal cooling mechanisms throughout the TC system. External cooling is modelled utilising a modified Goldstein correlation [74], with the effects of multiple film cooling flows accounted for using the Sellers superposition method [75].

Heat transfer through the solid is assessed as 1D conduction. Energy flow calculations are performed in the same manner as the coolant mass flow calculations but they must also consider the enthalpy of the fluid moving from inlet node i to outlet node j, which is set by the temperature of the inlet node, T_i, as well as the heat transfer from a solid node s to a fluid node i, which is determined by the temperature difference between the two nodes T_s - T_i and the compliance to the energy flow $E_{s,i}$. The compliances to heat flow are found from empirical correlations, such as the one in [76] used for impingement cooling. For a fluid node j connected to n fluid inlet nodes i, m outlet fluid nodes k and q solid nodes s, the energy flow is determined by solving for conservation of energy at each node using:

$$\sum_i^n \dot{m}_{i,j}h_i - \sum_k^m \dot{m}_{j,k}h_k + \sum_s^q \dot{Q}_{s,j} = \sum_i^n \dot{m}_{i,j}c_p T_i - \sum_k^m \dot{m}_{j,k}c_p T_j + \sum_s^q E_{s,i}(T_s - T_i) \tag{A2}$$

Film cooling is implemented differently to avoid the need to include the mainstream flow in the network. The driving temperature for external heat transfer, T_{aw}, is modified based on the temperature and Blowing Ratio $M = \rho_{cf}v_{cf}/\rho_\infty v_\infty$ of film hole flows upstream of each outer wall position (ρ_{cf},v_{cf} are coolant density and velocity at the film hole exit); this is done by using the modified Goldstein correlation [74] for film cooling effectiveness η_f, described by:

$$\eta_f = \frac{T_\infty - T_{aw}}{T_\infty - T_{c,e}} = \frac{Mu_\infty d_f}{8\alpha_t\left(\frac{x}{d_f} + x_{decay}\right)} exp\left(-\left(\frac{\left|\frac{z}{d_f}\right|}{c_1}\right)^2\right) \tag{A3}$$

where the coefficient values for α_t, x_{decay} and c_1 were based on the results of [8]. At high porosity, films from different holes are likely to interact; the effect of this is accounted for using Sellers' superposition method [75]. For a given position in the TC system of Fig. 4b which receives film cooling from n films, each with their own effectiveness η_{fi}, the overall film cooling effectiveness η_f is found by Eq ($A3$). As the entire TC array of Fig. 4b is analysed, all upstream data is available when evaluating film effectiveness, which can be performed simultaneously via the internal cooling evaluation by:

$$\eta_f = 1 - \prod_{i=1}^{n} \left(1 - \eta_{f_i}\right) \tag{A4}$$

Following the successful resolution of the network using Newton's iterative method, metal surface temperatures are obtained for the entire TC system in Fig. 4b based on the known nodal temperatures and energy flow compliances. These are then extracted for the unit cell in Fig. 4a chosen for subsequent stress analysis, i.e., associated with the stress code in Fig. 3c2, for which the average values throughout the hot and cold wall surfaces are used. A typical thermal conductivity value $k = 25$ W/m K for Nickel is used here, whereas the thermal conductivity and viscosity of air are made to vary with temperature using Sutherland's law.

B. Details of stress calculations of the LOM

The stress code of the LOM builds on the recent work by the authors in [9]. Here an extended version of the stress code is developed by incorporating the effect of effective plate stiffness reduction by the porosity. The isostrain condition used in Fig. 2c1, implies that: A) the inner/cooler plate constrains the expansion of the hotter/outer plate, inducing compressive forces $-N_x$,$-N_z$ on the latter and equal tensile forces on the former (satisfying equilibrium with zero applied external load), and, B) any thermal curvature of the outer wall due to the difference T_{max}-T_{med} is eliminated by opposing bending moments $-M_x$,$-M_z$ to ensure that the walls remain flat. Equal total strain between the two plates in the x and z directions (implication A) determines the forces via Eqs $A5(i)$-(ii) below, whereas zero total bending curvature in the outer plate in z and x directions (implication B) determines the moments via Eqs $A6(i)$-(ii).

$$-\frac{N_x}{{t_h}^2}\int_{-\frac{t_c}{2}}^{\frac{t_h}{2}} \widehat{S}_{11}(T(\xi))dy - \frac{N_z}{{t_h}^2}\int_{-\frac{t_c}{2}}^{\frac{t_h}{2}} \widehat{S}_{13}(T(\xi))dy + \frac{1}{t_h}\int_{-\frac{t_h}{2}}^{\frac{t_h}{2}} a(T(\xi))T(\xi)dy = \frac{N_x}{t_c}\widehat{S}_{11}(T_{min}) + \frac{N_z}{t_c}\widehat{S}_{13}(T_{min}) + aT_{min}\ (i) \tag{A5}$$

$$-\frac{N_x}{{t_h}^2}\int_{-\frac{t_c}{2}}^{\frac{t_h}{2}} \widehat{S}_{31}(T(\xi))dy - \frac{N_z}{{t_h}^2}\int_{-\frac{t_c}{2}}^{\frac{t_h}{2}} \widehat{S}_{33}(T(\xi))dy + \frac{1}{t_h}\int_{-\frac{t_h}{2}}^{\frac{t_h}{2}} a(T(\xi))T(\xi)dy = \frac{N_x}{t_c}\widehat{S}_{31}(T_{min}) + \frac{N_z}{t_c}\widehat{S}_{33}(T_{min}) + aT_{min}\ (ii)$$

$$-\frac{M_x}{I}\int_{-\frac{t_h}{2}}^{\frac{t_h}{2}} \widehat{S}_{11}(T(\xi))y^2dy - \frac{M_z}{I}\int_{-\frac{t_h}{2}}^{\frac{t_h}{2}} \widehat{S}_{13}(T(\xi))y^2dy + \int_{-\frac{t_h}{2}}^{\frac{t_h}{2}} \alpha(T(\xi))T(\xi)ydy = 0\ (i) \tag{A6}$$

$$-\frac{M_x}{I}\int_{-\frac{t_h}{2}}^{\frac{t_h}{2}} \widehat{S}_{31}(T(\xi))y^2dy - \frac{M_z}{I}\int_{-\frac{t_h}{2}}^{\frac{t_h}{2}} \widehat{S}_{33}(T(\xi))y^2dy + \int_{-\frac{t_h}{2}}^{\frac{t_h}{2}} \alpha(T(\xi))T(\xi)ydy = 0\ (ii)$$

$I = {t_h}^3/12$ is the second moment of area per unit length. $\widehat{S}_{ij}$ are components of the plate compliance matrix $\widehat{\boldsymbol{S}} = \overline{\boldsymbol{T}}^T\boldsymbol{S}\ \overline{\boldsymbol{T}}$ calculated by transformation of the material compliance matrix $\boldsymbol{S}$ onto the plate system xyz (11 and 33 correspond to x and z axes as detailed in [9] and [22]) as follows. We firstly define three compliance constants:

$$S_{11} = \frac{C_{11} + C_{12}}{(C_{11} - C_{12})(C_{11} + 2C_{12})},\ S_{12} = -\frac{C_{12}}{(C_{11} - C_{12})(C_{11} + 2C_{12})},\ S_{44} = \frac{1}{C_{44}} \tag{A7}$$

and associated material compliance:

$$\boldsymbol{S} = \begin{bmatrix} S_{11} & S_{12} & S_{12} & 0 & 0 & 0 \\ S_{12} & S_{11} & S_{12} & 0 & 0 & 0 \\ S_{12} & S_{12} & S_{11} & 0 & 0 & 0 \\ 0 & 0 & 0 & S_{44} & 0 & 0 \\ 0 & 0 & 0 & 0 & S_{44} & 0 \\ 0 & 0 & 0 & 0 & 0 & S_{44} \end{bmatrix} \tag{A8}$$

and then apply a transformation $\widehat{\boldsymbol{S}} = \overline{\boldsymbol{T}}^T\boldsymbol{S}\ \overline{\boldsymbol{T}}$ from the material system to the plate system xyz based on a φ, θ, ψ rotation sequence (in this study $\theta = \psi = 0$). $\overline{\boldsymbol{T}}$ is given by:

$$\overline{\boldsymbol{T}} = \begin{bmatrix} {T_{11}}^2 & {T_{12}}^2 & {T_{13}}^2 & 2T_{12}T_{13} & 2T_{11}T_{13} & 2T_{11}T_{12} \\ {T_{21}}^2 & {T_{22}}^2 & {T_{23}}^2 & 2T_{22}T_{23} & 2T_{21}T_{23} & 2T_{21}T_{22} \\ {T_{31}}^2 & {T_{32}}^2 & {T_{33}}^2 & 2T_{32}T_{33} & 2T_{31}T_{33} & 2T_{31}T_{32} \\ T_{21}T_{31} & T_{22}T_{32} & T_{23}T_{33} & T_{22}T_{33} + T_{23}T_{32} & T_{21}T_{33} + T_{23}T_{31} & T_{21}T_{32} + T_{22}T_{31} \\ T_{11}T_{31} & T_{12}T_{32} & T_{13}T_{33} & T_{12}T_{33} + T_{13}T_{32} & T_{11}T_{33} + T_{13}T_{31} & T_{11}T_{32} + T_{12}T_{31} \\ T_{11}T_{21} & T_{12}T_{22} & T_{13}T_{23} & T_{12}T_{23} + T_{13}T_{22} & T_{11}T_{23} + T_{13}T_{21} & T_{11}T_{22} + T_{12}T_{21} \end{bmatrix} \tag{A9}$$

where T_{ij} the components of $\boldsymbol{T}$ which is given by:

$$\boldsymbol{T} = \begin{bmatrix} \cos\varphi & -\sin\varphi & 0 \\ \sin\varphi & \cos\varphi & 0 \\ 0 & 0 & 1 \end{bmatrix} \cdot \begin{bmatrix} 1 & 0 & 0 \\ 0 & \cos\theta & -\sin\theta \\ 0 & \sin\theta & \cos\theta \end{bmatrix} \cdot \begin{bmatrix} \cos\psi & -\sin\psi & 0 \\ \sin\psi & \cos\psi & 0 \\ 0 & 0 & 1 \end{bmatrix} \tag{A10}$$

Both $\widehat{S}_{ij}$ and a depend on temperature and therefore on the position ξ through the upper plate thickness. Bulk thermal stresses in the absence of holes in the model of Fig. 3c1 are readily computed from the above forces and moments.

In order to compute effective stresses in the presence of holes (Fig. 3c2), we determine the corresponding effective forces and moments by using Eqs $A5$, $A6(i)$-(ii) again, with the difference that $\widehat{S}_{ij}$ are replaced by their effective/increased values $\widehat{S}_{ij}^{eff}$ given in Eqs $A11(i)$-(iii) below.

$$\begin{aligned} \widehat{S}_{11}^{eff} &= \widehat{S}_{11}\left(1+\phi+\frac{\psi_x Z}{\sqrt{\widehat{S}_{11}}}\right)\ (i) \\ \widehat{S}_{33}^{eff} &= \widehat{S}_{33}\left(1+\phi+\frac{\psi_z Z}{\sqrt{\widehat{S}_{33}}}\right)\ (ii) \end{aligned} \tag{A11}$$

$$\widehat{S}_{13}^{eff} = \widehat{S}_{31}^{eff} = \widehat{S}_{13} - \phi\sqrt{\widehat{S}_{11}\widehat{S}_{33}}\ (iii).$$

These equations are applied separately for each plate of Fig. 3c2 as each has different porosity and hole geometry. Porosities can be expressed as $\phi = \pi r_x r_z / 2\mathscr{A}$, where $\mathscr{A}$ is the representative unit cell area; r_x=0.6 mm and r_z=0.3 mm are the large and small radii of the elliptical film hole profile in the x-z plane, whereas r_x=r_z=r=0.3 mm is the radius of the circular impingement hole. $\psi_x = \frac{\pi r_z{}^2}{2A}$, $\psi_z = \frac{\pi r_x{}^2}{2A}$ are the directional film hole densities and $Z = \sqrt{\widehat{S}_{44} + 2\left(\sqrt{\widehat{S}_{11}\widehat{S}_{33}} + \widehat{S}_{13}\right)}$ is a material parameter; note that $\psi_z > \psi_x$ in the upper plate of Fig. 3c2, which explains the anisotropic change of effective properties, in contrast to ϕ which only causes isotropic changes. Eqs $A11(i)$-(iii) can be recovered from the work of Tsukrov–Kachanov [52] for the case of an orthotropic material in the x-z plane consisted of parallel non-interacting elliptical cavities; cavity interaction can be included by normalising the terms $\phi + \frac{\psi_x Z}{\sqrt{\widehat{S}_{11}}}$ and $\phi + \frac{\psi_z Z}{\sqrt{\widehat{S}_{33}}}$ over the factor $1 - \phi$, consistent with the Mori-Tanaka scheme [53].

C. *Details of crystal plasticity finite element (CPFE) code*

We utilise here the CPFE methodology developed recently by the authors for single crystal Nickel based transpiration cooling blades [22], which also is affiliated with the Oxford-UMAT code presented in [77]. Since the overall methodology is established, here only a brief description is given. A distinguishing feature of our implementation here is that the change of the material stiffness over each increment of the analysis is also involved in the calculations, otherwise the enhancement of residual stress during cooldown due to the temperature dependence of elastic constants (Section 3.2) cannot be accurately captured. Assuming one-dimension for brevity here, the stress increment is written as $\sigma = E_{t+\Delta t}\Delta\varepsilon_{el} + \varepsilon_{elt}\Delta E$, where $E_{t+\Delta t}$ is the Young's modulus at the end of the increment ($t \rightarrow t + \Delta t$), $\Delta\varepsilon_{el}$ and ΔE are the changes in elastic strain and Young's modulus during the increment, respectively, and ε_{elt} is the elastic strain at the beginning of the increment.

Fig. 3c2 consists of approximately 40,000 linear tetrahedral elements (ABAQUS code: C3D4T), with an increased mesh density around the film and impingement holes to ensure mesh insensitive results. The isostrain constraint between the two plates is enforced by applying symmetry conditions at one of the two boundaries normal to the z axis (z_1 in Fig. 3c2) and postulating common z-displacement at the other boundary (z_2 in Fig. 3c2) where $\sigma_{CF_z}^*$ applies; the boundaries normal to the x axis must also satisfy periodicity, which is enforced by postulating that all the opposite node pairs exhibit the same relative x-displacement. Centrifugal loading is applied by the traction $\sigma_{CF_z}^*$ at the net sections of the walls. Thermal loading is applied by prescribing temperature in every element of the mesh (not only surface elements) to eliminate any transient effects when temperature cycling is used. The in-phase thermal-centrifugal load cycles of trapezoidal shape in the inset Fig. 6a' used in CPFE analysis involve startup and shutdown periods of 10 min and a steady-state period of 3 h.

While the elastic FE analysis of the stress code in Fig. 3c1 only requires the temperature dependent elastic constants C_{11}, C_{12}, C_{44} and thermal expansion coefficient a given here in Fig. 2a for the Nickel superalloy CMSX-4, the CPFE analysis also requires the constitutive law that determines the plastic and creep deformation rates shown respectively in Fig. 2b and c as a function of stress, temperature and orientation of stress in the material system, developed in [22]. Single crystal systems, in particular, necessitate the use of both temperature sensitive and orientation sensitive (anisotropic) plastic flow rules based on the Crystal Plasticity framework, rather than purely empirical isotropic flow rules, i.e. the widely used Johnson-Cook model [78]. The plastic and creep rates are expressed in terms of crystallographic slip rates $\dot{\gamma}^a$ (1/s) for each of the 12 octahedral <110>{111} and 6 cubic <110>{100} slip systems of Nickel superalloys that are listed in Table A1, by deploying our recently developed phenomenological plastic-creep law:

$$\begin{aligned} \dot{\gamma}^a \quad = \quad & \dot{\gamma}_0\left(\frac{|\tau^a|}{\tau_c^a(T)}\right)^{m_1 T + m_2} sign(\tau^a) \\ & + \left(\frac{\varkappa|\tau^a|}{1+\varkappa|\tau^a|}\right)^{\xi}\left\{\dot{\mathscr{S}}_o(T)exp\left(\mathscr{S}_\sigma(T)|\tau^a| - \frac{Q_{\mathscr{S}}}{RT}\right) + \Omega_o(T)exp\left(\Omega_\sigma|\tau^a| - \frac{Q_\Omega}{RT}\right)\gamma^a\right\}sign(\tau^a) \end{aligned} \tag{A12}$$

where τ^a (MPa) is the applied shear stress resolved on each system a (depends on the macroscopic stress tensor and its orientation in the material system), T is the temperature in Kelvin and γ^a is the slip already accumulated in the material. Except for the parameters $\varkappa$, ξ that are used for numerical convergence reasons, the rest of the parameters are material constants with the most important being the critical resolved shear stress $\tau_c^a(T)$ (MPa) which depends strongly on temperature and is directly proportional to the macroscopic yield stress $\sigma_y(T)$

as indicated in Fig. 2b. The $\tau_c^a(T)$ function for octahedral and cubic slip families, along with all these parameters are all given in Table 2. Eq (A12) involves the addition of two terms which capture different microstructural processes: the 1st term multiplied by $sign(\tau^a)$ predicts rate dependent yield/plasticity which dominates when stresses approach/reach yield, i.e. $\tau^a \to \tau_c^a(T)$ (or macroscopically $\sigma \to \sigma_y(T)$), related to the monotonic stress-strain response in Fig. 2b, whereas the 2nd term multiplied by $sign(\tau^a)$) captures high temperature creep which becomes significant at T>700 °C, related to the steady-stress creep data in Fig. 2c. For the purposes of this study, the phenomenological slip rule used here (Eq. (A12)) is considered advantageous over physically based creep laws [69,79] which present inherent numerical difficulties in modelling stress relaxation and cyclic inelastic deformation across the full temperature range 20–1100 °C.

Table A1
Octahedral and cubic slip systems used in the CPFE analysis and life assessment.

slipsystemtype	slipsystemno. a	slipdirection s^a	slipnormal n^a	SchmidfactorSF <001> loading	SchmidfactorSF <011> loading	SchmidfactorSF <111> loading
octahedral<110>{111}	1	$[1/\sqrt{2}\ -1/\sqrt{2}\,0]$	$[1/\sqrt{3}\,1/\sqrt{3}\,1/\sqrt{3}]$	$-1/\sqrt{6}$	0	0
	2	$[0\,1/\sqrt{2}\ -1/\sqrt{2}]$	$[1/\sqrt{3}\,1/\sqrt{3}\,1/\sqrt{3}]$	$1/\sqrt{6}$	$1/\sqrt{6}$	$2/3\sqrt{6}$
	3	$[1/\sqrt{2}\,0\,-1/\sqrt{2}]$	$[1/\sqrt{3}\,1/\sqrt{3}\,1/\sqrt{3}]$	0	$-1/\sqrt{6}$	$-2/3\sqrt{6}$
	4	$[1/\sqrt{2}\,1/\sqrt{2}\,0]$	$[-1/\sqrt{3}\,1/\sqrt{3}\,1/\sqrt{3}]$	$-1/\sqrt{6}$	0	0
	5	$[0\,1/\sqrt{2}\ -1/\sqrt{2}]$	$[-1/\sqrt{3}\,1/\sqrt{3}\,1/\sqrt{3}]$	$1/\sqrt{6}$	$1/\sqrt{6}$	0
	6	$[1/\sqrt{2}\,0\,1/\sqrt{2}]$	$[-1/\sqrt{3}\,1/\sqrt{3}\,1/\sqrt{3}]$	0	$-1/\sqrt{6}$	0
	7	$[1/\sqrt{2}\,1/\sqrt{2}\,0]$	$[1/\sqrt{3}\ -1/\sqrt{3}\,1/\sqrt{3}]$	$-1/\sqrt{6}$	0	$2/3\sqrt{6}$
	8	$[0\,1/\sqrt{2}\,1/\sqrt{2}]$	$[1/\sqrt{3}\ -1/\sqrt{3}\,1/\sqrt{3}]$	$1/\sqrt{6}$	0	$-2/3\sqrt{6}$
	9	$[1/\sqrt{2}\,0\,-1/\sqrt{2}]$	$[1/\sqrt{3}\ -1/\sqrt{3}\,1/\sqrt{3}]$	0	0	0
	10	$[1/\sqrt{2}\ -1/\sqrt{2}\,0]$	$[1/\sqrt{3}\,1/\sqrt{3}\ -1/\sqrt{3}]$	$-1/\sqrt{6}$	0	$-2/3\sqrt{6}$
	11	$[0\,1/\sqrt{2}\,1/\sqrt{2}]$	$[1/\sqrt{3}\,1/\sqrt{3}\ -1/\sqrt{3}]$	$1/\sqrt{6}$	0	0
	12	$[1/\sqrt{2}\,0\,1/\sqrt{2}]$	$[1/\sqrt{3}\,1/\sqrt{3}\ -1/\sqrt{3}]$	0	0	$2/3\sqrt{6}$
cubic<110>{100}	13	$[0\,1/\sqrt{2}\,1/\sqrt{2}]$	[100]	0	0	$2/3\sqrt{2}$
	14	$[0\,1/\sqrt{2}\ -1/\sqrt{2}]$	[100]	0	0	0
	15	$[1/\sqrt{2}\,0\,1/\sqrt{2}]$	[010]	0	$-1/2\sqrt{2}$	0
	16	$[1/\sqrt{2}\,0\,-1/\sqrt{2}]$	[010]	0	$1/2\sqrt{2}$	$-2/3\sqrt{2}$
	17	$[1/\sqrt{2}\,1/\sqrt{2}\,0]$	[001]	0	$1/2\sqrt{2}$	0
	18	$[1/\sqrt{2}\ -1/\sqrt{2}\,0]$	[001]	0	$-1/2\sqrt{2}$	$-2/3\sqrt{2}$

D. *Fatigue life model*

D1. *Description of fatigue life calculation used in Fig. 7d*

Integration of Eq (A12) over the time duration t_c of the thermal-centrifugal cycles in Fig. 6a', provides the slip accumulation per cycle $\widetilde{\gamma}_c = \int_0^{t_c} max|\dot{\gamma}^a|dt$ at the critical hole location operating in the fatigue regime. Slip in the most dominant slip system ($max|\dot{\gamma}^a|$) is only integrated since fatigue crack initiation is driven by a single slip process [68]), and the absolute value is integrated because $\dot{\gamma}^a$ changes sign between the two extremes of the load cycle for the hot spot location that operates in the fatigue regime. The two $\widetilde{\gamma}_c$-N_f relationships in Fig. 6b are derived from the experimental $\Delta\varepsilon$-N_f results of uniaxial strain controlled isothermal fatigue experiments on the CMSX-4 Nickel superalloy ($\Delta\varepsilon$=applied cyclic total strain range) along the $\langle 111\rangle$ and $\langle 001\rangle$ crystal orientations, presented in [55]. For each orientation, we determine the inelastic part of $\Delta\varepsilon$ as $\Delta\varepsilon_p = \Delta\varepsilon - \Delta\sigma/E$ ($\Delta\sigma$=saturated cyclic stress range $\Delta\sigma$, E=orientation dependent Young's modulus) and then use $\widetilde{\gamma}_c = 2\Delta\varepsilon_p/nSF$ (n=number of active slip systems, SF =Schmid factor). For the $\langle 111\rangle$ tests we consider that cubic slip dominates ($n = 3$, $SF = 0.4714$) whereas for the $\langle 001\rangle$ tests only octahedral slip occurs i.e., $n = 8$, $F = 0.4082$.

D2. *Justification of fatigue life calculation described in D1*

The cycles N_f required for low cycle fatigue crack initiation are commonly considered to obey the empirical Manson-Coffin relation $\Delta\varepsilon_p = f_1 N_f^{f_2}$, where $\Delta\varepsilon_p$ is the cyclic plastic strain range and f_1, f_2 material constants [56]. However, since the total strain range $\Delta\varepsilon$ is the usual controlling variable in fatigue experiments, the above is typically combined with power laws for high cycle fatigue e.g. the Basquin law, in order to relate N_f with $\Delta\varepsilon$ instead of $\Delta\varepsilon_p$ [36,55]. Extensions have been used to capture temperature, loading orientation and mean stress effects [36,55,80]. A limitation of all these schemes is that they do not describe the data in terms of the slip quantities that drive crack initiation and therefore lack in capturing the various effects surrounding fatigue in a compact and physical manner. For example, the fatigue life of Nickel superalloys degrades as the orientation changes from $\langle 001\rangle$ to $\langle 011\rangle$ to $\langle 111\rangle$ and as the temperature T increases [73], such that for each orientation and each T a different $\Delta\varepsilon - N_f$ relation must be fitted to capture the data [55]. However, by replacing $\Delta\varepsilon$ with the slip range $\Delta\gamma$, all the data can be collapsed into a single power law curve $\Delta\gamma = f_1 N_f^{f_2}$ [81], indicating that fatigue degrades with increasing T and Young's modulus E (E increases from $\langle 001\rangle$ to <111) mainly because both of these imply more slip per cycle for the same applied $\Delta\varepsilon$ (T reduces yield stress) [73]. A further discussion on various versions of slip based fatigue laws is available in [82].

A limitation of strain range measures is that they are unable to represent fatigue damage under complex cyclic loading histories [83] whereby inelastic strain can occur in more than two instances through the cycle. This has been addressed by time incremental damage rules in which both the RSS and slip rate $\dot{\gamma}^i$ are integrated through the cycle [83,84]. These rules have also been combined with creep damage rules to capture synergistic creep-fatigue damage effects. Tinga et al. [83] proposed one such rule for CMSX-4 and provided a physical basis for the quantities integrated through the cycle; however, they calibrated 8 material constants based on a small fatigue data set of isothermal tests at 850 °C and <001>. A similar procedure was followed by Levkovitch et al. [84] who used a simpler law with 6 constants for CMSX-4 based on isothermal fatigue data for 950 °C and mainly ⟨001⟩.

The above suggest that a comprehensive, physically based fatigue law that captures data in a wide range of orientations and temperatures is not available. Developing one such law is not our objective here. However, our fatigue life calculation described in Appendix D1 incorporates the advantages of time incremental laws and slip based laws while also accounting for the fatigue data reported in [55] for both ⟨001⟩ and ⟨111⟩ in the relatively wide temperature range of 850–1050 °C. The merit of our fatigue life model is that it converts $\Delta\varepsilon - N_f$ data into $\widetilde{\gamma}_c - N_f$ data. The quality of fit (see R^2 values in Fig. 6b) indicates that fatigue data at different temperatures collapse well onto the same $\widetilde{\gamma}_c - N_f$ curve. Lukas et al. [81] showed that the same should occur between orientations, i.e. a single relationship based on octahedral slip should have captured all the data in Fig. 6b. However, this cannot be the case here due to the presence of cubic slip, which was necessary in this study in order to capture the lower yield stress along ⟨111⟩ through a Schmid based constitutive law [85]. On the other hand, the results by Lukas et al. were specific to 700 °C [81] and controversy still remains surrounding the role of cubic slip in deformation mechanisms at various temperatures [85].

D3. Discussion on the effect of creep on fatigue life

Time dependent (creep) deformation and damage plays a crucial role in fatigue failure in the sense that slow loading-unloading strain rates $\dot{\varepsilon}$ result in less cycles to failure N_f than high rates $\dot{\varepsilon}$, and N_f decreases further if a creep dwell is included [80,83]. Tinga et al. [83] showed that if fatigue data from slow and fast load cycles with varying creep dwell times are put together in a failure time versus failure cycles $t_f - N_f$ plot, they obey a non-linear relationship due to the creep-fatigue interaction. From a microstructural viewpoint we can argue that creep enhances low cycle fatigue failure in the sense that creep deformation can contribute to the fatigue damage process and the growth and coalescence of voids provides internal free surfaces where dislocations can escape and enhance the irreversibility of slip. Inversely, we can argue that fatigue enhances creep on the basis that immobilized dislocation segments generated by load reversals promote the growth and coalescence of voids [83]. The above interactions suggest that the non-linear $t_f - N_f$ relation cannot be captured by traditional damage rules where independent creep and fatigue contributions are simply added, e.g. $D = D_{cr} + D_{fat}$, and for this reason Tinga et al. [83] added an interaction term $I_{int}\frac{D_{cr}D_{fat}}{D_{cr}+D_{fat}}$. A value of $I_{int} = 3.5$ was required to fit CMSX-4 data, suggesting a strong creep-fatigue interaction.

The effect of creep deformation on fatigue life can also be identified in the context of a local cyclic plastic shakedown state. For example, if slower temperature cycles are used in Fig. 6a', then plasticity (thermally activated glide) will occur at lower yield stresses which for displacement controlled loading implies more slip accumulation and thus lower N_f [80]. In addition, more creep strain will occur at high temperature which will influence the amount of plasticity experienced in the opposite direction on unloading. Similarly, if the creep dwell period increases then both the creep strain at high temperature and the plastic strain on unloading will increase, again reducing N_f [80]. The effect of creep dwell and stress relaxation on plasticity during unloading is described in detail by the authors in [56].

This second viewpoint (and not the first microstructural viewpoint) suggests that time dependent damage and the so-called 'creep-fatigue interaction' effect, i.e., the effect of creep on fatigue life, are inevitably present in our results and fatigue life calculation described in Appendix D1. Our fatigue life model captures by definition the strong nonlinear nature of the $t_f - N_f$ relationship presented by Tinga et al. [83] without requiring the addition of a creep damage term as well as the addition and calibration of a creep-fatigue interaction term; this was verified here via preliminary single element cyclic simulations at different $\dot{\varepsilon}$ rates and creep dwell times.

Data availability

Data will be made available on request.

References

[1] Padture NP. Advanced structural ceramics in aerospace propulsion. Nat Mater 2016;15(8):804–9.
[2] Pollock TM. Alloy design for aircraft engines. Nat Mater 2016;15(8):809–15.
[3] Eswarappa Prameela S, et al. Materials for extreme environments. Nature Reviews Materials 2023;8(2):81–8.
[4] Krewinkel R. A review of gas turbine effusion cooling studies. Int J Heat Mass Transf 2013;66:706–22.
[5] Zhang J, et al. Recent advances in film cooling enhancement: a review. Chin J Aeronaut 2020;33(4):1119–36.
[6] Mi Q, et al. Research progress of transpiration cooling for aircraft thermal protection. Appl Therm Eng 2023:121360.
[7] Murray AV, et al. High resolution experimental and computational methods for modelling multiple row effusion cooling performance. Int J Turbomach, Propuls Power 2018;3(1):4.
[8] Courtis M, et al. Influence of spanwise and streamwise film hole spacing on adiabatic film effectiveness for effusion-cooled gas turbine blades. Int J Turbomach, Propuls and Power 2021;6(3):37.
[9] Courtis M, et al. Coupled aerothermal-mechanical analysis in single crystal double wall transpiration cooled gas turbine blades with a large film hole density. Appl Therm Eng 2022;219(A):119329.
[10] Ngetich GC, et al. A three-dimensional conjugate approach for analyzing a double-walled effusion-cooled turbine blade. J Turbomach 2019;141(1).
[11] Luan Y, et al. Research for double wall cooling configuration with flower shaped ribs. Int J Thermal Sci 2023;193:108493.
[12] Chen Y, Wei H, Zu Y. Experimental study on the conjugate heat transfer of double-wall turbine blade components with/without pins. Thermal Sci Eng Progr 2018;8:448–56.
[13] Pu J, Zhang T, Wang J-h. Experimental study of cooling air effect on overall cooling of laminated configuration at a turbine vane end-wall. Case Stud Thermal Eng 2022;32:101890.
[14] Pu J, et al. Visualization and quantitation of unsteadiness of film cooling near stagnation line of a double-wall cooled vane leading edge. J Vis (Tokyo) 2023;26(1):113–29.
[15] Coulton B, Murray AV, Ireland PT. A computational approach to aerothermal analysis of complex internal turbine cooling geometries. Turbo expo: power for land, sea, and air. American Society of Mechanical Engineers; 2022.
[16] Murray AV, et al. The manufacturing and experimental validation of a nickel superalloy double-wall, effusion test specimen. Turbo expo: power for land, sea, and air. American Society of Mechanical Engineers; 2023.
[17] Skamniotis C, Courtis M, Cocks AC. Multiscale analysis of thermomechanical stresses in double wall transpiration cooling systems for gas turbine blades. Int J Mech Sci 2021;207:106657.
[18] Skamniotis C, Cocks AC. 2D and 3D thermoelastic phenomena in double wall transpiration cooling systems for gas turbine blades and hypersonic flight. Aerosp Sci Technol 2021;113:106610.
[19] Skamniotis C, Cocks AC. Thermal and centrifugal stresses in curved double wall transpiration cooled components with temperature dependent thermoelastic properties. Int J Solids Struct 2022;234:111273.
[20] Skamniotis C, Cocks AC. Designing against severe stresses at compound cooling holes of double wall transpiration cooled engine components. Aerosp Sci Technol 2021;116:106856.
[21] Skamniotis C, Cocks AC. Creep-plasticity-fatigue calculations in the design of porous double layers for new transpiration cooling systems. Int J Fatigue 2021;151:106304.
[22] Skamniotis C, Grilli N, Cocks AC. Crystal plasticity analysis of fatigue-creep behavior at cooling holes in single crystal Nickel based gas turbine blade components. Int J Plast 2023;166:103589.
[23] van de Noort M, Ireland PT, Telisinghe JC. Effects of manufacturing tolerances on double-wall effusion cooling. J Turbomach 2024;146(1):1–10.
[24] van de Noort M, Ireland P. A low order flow network model for double-wall effusion cooling systems. Int J Turbomach, Propuls Power 2022;7(1):5.
[25] Murray AV, Ireland PT, Romero E. Development of a steady-state experimental facility for the analysis of double-wall effusion cooling geometries. J Turbomach 2019;141(4):041008.
[26] Murray AV, Ireland PT, Romero E. Experimental and computational methods for the evaluation of double-wall, effusion cooling systems. J Turbomach 2020;142(11):111003.

[27] Dong Z, et al. Optimization of film cooling arrays on a gas turbine vane by using an integrated approach of numerical simulation and parameterized design. Appl Therm Eng 2023;219:119464.

[28] Kim M, et al. Experimental investigation of effusion and transpiration air cooling for single turbine blade. Appl Therm Eng 2021;182:116156.

[29] Kim KM, et al. Optimal design of impinging jets in an impingement/effusion cooling system. Energy 2014;66:839–48.

[30] Wang J, et al. An experimental investigation on transpiration cooling of wedge shaped nose cone with liquid coolant. Int J Heat Mass Transf 2014;75:442–9.

[31] Wang M, et al. Correction formula for film-cooling effectiveness considering the influence of thermal radiation in high-temperature environments. Appl Therm Eng 2023;222:119903.

[32] Xiao X, et al. Large-eddy simulation of transpiration cooling in turbulent channel with porous wall. Appl Therm Eng 2018;145:618–29.

[33] Zhou Z-J, et al. Effect of skew angle of holes on the thermal fatigue behavior of a Ni-based single crystal superalloy. Acta Metallur Sin (Engl Lett) 2017;30(2): 185–92.

[34] Zhou H, et al. Crystal plasticity analysis of cylindrical holes and their effects on the deformation behavior of Ni-based single-crystal superalloys with different secondary orientations. Int J Plast 2019;119:249–72.

[35] Wang J, et al. The inter-hole interference on creep deformation behavior of nickel-based single crystal specimen with film-cooling holes. Int J Mech Sci 2019;163: 105090.

[36] Guo Z, et al. Experimental and analytical investigation on service life of film cooling structure for single crystal turbine blade. Int J Fatigue 2021;150:106318.

[37] Wen Z, et al. A combined CP theory and TCD for predicting fatigue lifetime in single-crystal superalloy plates with film cooling holes. Int J Fatigue 2018;111: 243–55.

[38] Wen Z, et al. Prediction method for creep life of thin-wall specimen with film cooling holes in Ni-based single-crystal superalloy. Int J Mech Sci 2018;141: 276–89.

[39] Sun W, et al. Effect of film-hole configuration on creep rupture behavior of a second generation nickel-based single crystal superalloys. Mater Charact 2017;130: 298–310.

[40] Li Z, et al. Investigation on high temperature fatigue-oxidation behavior of Ni-based single crystal with film cooling holes considering arrangement effect. Eng Fract Mech 2024;307:110326.

[41] Li F, et al. Fatigue life estimation of nickel-based single crystal superalloy with different inclined film cooling holes: initial damage quantification and coupling of damage-fracture mechanics models. Int J Plast 2024;176:103967.

[42] Skamniotis C, Cocks AC. Analytical shakedown, ratchetting and creep solutions for idealized twin-wall blade components subjected to cyclic thermal and centrifugal loading. Eur J Mech-A/Solids 2022:104652.

[43] Skamniotis C, Cocks AC. Minimising stresses in double wall transpiration cooled components for high temperature applications. Int J Mech Sci 2021;189:105983.

[44] Skamniotis C, Cocks AC. Ratchetting and creep failure in twin-wall turbine blades experiencing severe thermal and centrifugal loading. J Appl Mech 2022;89(9): 091005.

[45] Murray AV, Ireland PT, Rawlinson AJ. An integrated conjugate computational approach for evaluating the aerothermal and thermomechanical performance of double-wall effusion cooled systems. Turbo expo: power for land, sea, and air. American Society of Mechanical Engineers; 2017.

[46] Epishin A, et al. Investigation of elastic properties of the single-crystal nickel-base superalloy CMSX-4 in the temperature interval between room temperature and 1300 °C. Crystals (Basel) 2021;11(2):152.

[47] Dye D, et al. Welding of single crystal superalloy CMSX-4: experiments and modeling. In: Superalloys 2004 (Tenth International Symposium); 2004.

[48] Allan CD. Plasticity of nickel base single crystal superalloys. Massachusetts Institute of Technology; 1995.

[49] Zhu Z, et al. A model for the creep deformation behaviour of nickel-based single crystal superalloys. Acta Mater 2012;60(12):4888–900.

[50] van de Noort M, Murray AV, Ireland PT. Low order heat & mass flow network modelling for quasi-transpiration cooling systems. Turbo expo: power for land, sea, and air. American Society of Mechanical Engineers; 2022.

[51] Courtis M, Ireland P. Influence of porosity on double-walled effusion-cooled systems for gas turbine blades. Turbo expo: power for land, sea, and air. American Society of Mechanical Engineers; 2022.

[52] Tsukrov I, Kachanov M. Effective moduli of an anisotropic material with elliptical holes of arbitrary orientational distribution. Int J Solids Struct 2000;37(41): 5919–41.

[53] Kachanov, M., I. Tsukrov, and B. Shafiro, *Effective moduli of solids with cavities of various shapes.* 1994.

[54] Rodopoulos DC, Karathanasopoulos N. Thermally and mechanically induced strain gradient fields in architected 2D materials and beam structures. Int J Solids Struct 2024;288:112603.

[55] Scholz A, et al. Modeling of mechanical properties of alloy CMSX-4. Mater Sci Eng: A 2009;510:278–83.

[56] Skamniotis CG, Cocks AC. Creep-plasticity-fatigue calculations in the design of porous double layers for new transpiration cooling systems. Int J Fatigue 2021: 106304.

[57] Ince A, Glinka G, Buczynski A. Computational modeling of multiaxial elasto-plastic stress–strain response for notched components under non-proportional loading. Int J Fatigue 2014;62:42–52.

[58] Peigney M. Shakedown of elastic-perfectly plastic materials with temperature-dependent elastic moduli. J Mech Phys Solids 2014;71:112–31.

[59] Hasbroucq S, Oueslati A, de Saxcé G. Inelastic responses of a two-bar system with temperature-dependent elastic modulus under cyclic thermomechanical loadings. Int J Solids Struct 2010;47(14–15):1924–32.

[60] Ma Z, et al. A unified direct method for ratchet and fatigue analysis of structures subjected to arbitrary cyclic thermal-mechanical load histories. Int J Mech Sci 2021;194:106190.

[61] Qiu, K., et al., *Temperature Dependent Elasticity Enhances Residual Stresses and Ratcheting: a Shakedown Analysis in Double Wall Transpiration Cooled Single Crystal Nickel Gas Turbine Blades.* Available at SSRN 5069972.

[62] Heuer S, et al. Aiming at understanding thermo-mechanical loads in the first wall of DEMO: stress–strain evolution in a Eurofer-tungsten test component featuring a functionally graded interlayer. Fusion Eng Design 2018;135:141–53.

[63] Zhou G, et al. The European DEMO helium cooled pebble bed breeding blanket: design status at the conclusion of the pre-concept design phase. Energies (Basel) 2023;16(14):5377.

[64] Skamniotis C, et al. On the effect of nuclear fission cladding stresses on Zirconium hydride orientation and dislocation strain energy fields via discrete dislocation plasticity and crystal plasticity finite element modelling. J Mech Phys Solids 2025; 195:105924.

[65] Thurman D, et al. Investigation of spiral and sweeping holes. J Turbomach 2016; 138(9):091007.

[66] Xu Z, et al. Tension-compression asymmetry of nickel-based superalloys: a focused review. J Alloys Compd 2023;945:169313.

[67] Leidermark D, et al. Tension/compression asymmetry of a single-crystal superalloy in virgin and degraded condition. Acta Mater 2010;58(15):4986–97.

[68] Leidermark D, et al. A combined critical plane and critical distance approach for predicting fatigue crack initiation in notched single-crystal superalloy components. Int J Fatigue 2011;33(10):1351–9.

[69] Karamitros V, MacLachlan DW, Dunne FP. Modelling of short crack growth in single crystal Ni $\gamma - \gamma'$ microstructure. Acta Mater 2022;240:118305.

[70] Liu H, et al. A numerical approach to simulate 3D crack propagation in turbine blades. Int J Mech Sci 2020;171:105408.

[71] Li S, et al. Low-temperature hot corrosion effects on the low-cycle fatigue lifetime and cracking behaviors of a powder metallurgy Ni-based superalloy. Int J Fatigue 2018;116:334–43.

[72] Gudivada G, Pandey AK. Recent developments in nickel-based superalloys for gas turbine applications. J Alloys Compd 2023:171128.

[73] Reed RC. The superalloys: fundamentals and applications. Cambridge university press; 2008.

[74] Goldstein RJ. Film cooling. Advances in heat transfer. Elsevier; 1971. p. 321–79.

[75] Sellers Jr JP. Gaseous film cooling with multiple injection stations. AIAA J 1963;1 (9):2154–6.

[76] San J-Y, Shiao W-Z. Effects of jet plate size and plate spacing on the stagnation Nusselt number for a confined circular air jet impinging on a flat surface. Int J Heat Mass Transf 2006;49(19–20):3477–86.

[77] Demir E, et al. OXFORD-UMAT: an efficient and versatile crystal plasticity framework. Int J Solids Struct 2025;307:113110.

[78] Pandya KS, Roth CC, Mohr D. Strain rate and temperature dependent fracture of aluminum alloy 7075: experiments and neural network modeling. Int J Plast 2020; 135:102788.

[79] Skamniotis C, et al. On the interaction of grain-scale and hydride-scale stresses in hydrogen enriched zirconium alloy nuclear cladding via combined discrete dislocation plasticity and crystal plasticity finite element modelling. Mech Mater 2024;195:105033.

[80] MacLachlan D, Knowles D. Fatigue behaviour and lifing of two single crystal superalloys. Fatigue Fract Eng Mater Struct 2001;24(8):503–21.

[81] Lukas P, et al. Fatigue and creep of superalloy single crystals CMSX-4. Kovové Mater 1998;36:205–12.

[82] Arakere NK, Swanson G. Effect of crystal orientation on fatigue failure of single crystal nickel base turbine blade superalloys. Turbo expo: power for land, sea, and air. American Society of Mechanical Engineers; 2000.

[83] Tinga T, Brekelmans W, Geers M. Time-incremental creep–fatigue damage rule for single crystal Ni-base superalloys. Mater Sci Eng: A 2009;508(1–2):200–8.

[84] Levkovitch V, Sievert R, Svendsen B. Simulation of deformation and lifetime behavior of a fcc single crystal superalloy at high temperature under low-cycle fatigue loading. Int J Fatigue 2006;28(12):1791–802.

[85] Fedelich B. *Crystal plasticity models: dislocation based,* in *nickel base single crystals across length scales.* Elsevier; 2022. p. 401–27.